



FULL PAPER

Open Access



Numerical simulations to explain the coseismic electromagnetic signals: a case study for a *M*5.4 aftershock of the 2016 Kumamoto earthquake

Yao-Chong Sun¹ , Makoto Uyeshima², Hengxin Ren^{1*} , Qinghua Huang³, Koki Aizawa⁴, Kaori Tsukamoto^{5,6}, Wataru Kanda⁷, Kaori Seki^{7,8}, Takahiro Kishita^{7,9}, Takao Ohminato², Atsushi Watanabe², Jiangjun Ran¹ and Xiaofei Chen¹

Abstract

Coseismic electromagnetic (EM) signals that appear from the P arrival were observed in a volcanic area during the 2016 Kumamoto earthquake. In this study, we conduct numerical simulations to explain the coseismic EM signals observed for a *M*5.4 aftershock of the earthquake. Initially, we adopt a water-saturated half-space model, and its simulation result for a receiver with a depth of 0.1 m suggests that the magnetic signals do not show up at the arrivals of P, refracted SV–P and Rayleigh waves because the evanescent EM waves just counterbalance the localized magnetic signals that accompany P, refracted SV–P and Rayleigh waves. Then, we conduct numerical simulations on a seven-layer half-space model in which the second layer corresponds to an aquifer analogy and the six other layers refer to air-saturated porous media. When only the electrokinetic effect is considered, the simulated coseismic magnetic signals still appear from the S arrival. The combination of electrokinetic effect and surface-charge assumption is also tested. We find that signals before the S arrival are missing on the transverse seismic, transverse electric, radial magnetic and vertical magnetic components, although the situation on horizontal magnetic components is improved to an extent. Then, we introduce an artificial scattering effect into our numerical simulations given that the scattering effect should exist in the volcanic area. New numerical result shows good agreement with the observation result on the signal appearance time. Hence, the combination of electrokinetic and scattering effects is a plausible explanation of coseismic EM signals. Further investigations indicate that coseismic electric and/or magnetic signals are more sensitive to the scattering effect and the aquifer thickness than seismic signals.

Keywords: Coseismic EM signals, 2016 Kumamoto earthquake, Numerical simulation, Electrokinetic effect, Scattering effect

Introduction

The existence of the seismo-electromagnetic phenomena has been confirmed by field observations in previous decades (Johnston and Mueller 1987; Mueller and Johnston

1990; Fujinawa et al. 2011; Han et al. 2011, 2014, 2015, 2016, 2017; Huang 2011a, b; Hattori et al. 2013; Xu et al. 2013; Fujinawa and Noda 2015; Wang and Huang 2016; Liu et al. 2017; Sakai et al. 2017). Among these phenomena, the most frequently reported is coseismic electromagnetic (EM) signals. In contrast with the direct magnetic signals that show up almost at earthquake origin time (Okubo et al. 2011), coseismic EM signals show up simultaneously with seismic arrivals (Honkura et al.

*Correspondence: renhx@sustech.edu.cn

¹ Department of Earth and Space Sciences, Southern University of Science and Technology, Shenzhen, Guangdong 518055, China
Full list of author information is available at the end of the article

2000; Nagao et al. 2000; Skordas et al. 2000; Karakelian et al. 2002a, b; Tang et al. 2010; Matsushima et al. 2013; Tsutsui 2014; Gao et al. 2016). This phenomenon may imply some principle of the relationship between natural earthquakes and anomalous EM signals. Therefore, this phenomenon has attracted the attention of many researchers, and related theoretical studies have been conducted (Gershenzon et al. 1993; Ogawa and Utada 2000; Huang 2002; Honkura et al. 2009; Yamazaki 2012, 2013). However, the complexity of the real earth model has presented a tough challenge and the progress of theoretical studies is somewhat slow. At present, our understanding with regard to coseismic EM signals is still insufficient, and this case has limited the application of the recorded data in seismic hazard research.

A possible and widely accepted generation mechanism is the electrokinetic effect (Mizutani et al. 1976; Gershenzon et al. 1993, 2014; Johnston 1997; Fujinawa et al. 2011; Mahardika et al. 2012; Fujinawa and Noda 2015), which takes place in porous media because of the existence of the electric double layer (Frenkel 1944; Davis et al. 1978). The electrokinetic effect can result in seismic-to-EM energy conversion, which is often called seismoelectric conversion. This effect may be responsible for both coseismic and pre-seismic EM phenomena. Numerical simulation studies on the electrokinetically induced coseismic EM signals have been conducted (Hu and Gao 2011; Ren et al. 2012, 2015, 2016a, b; Zhang et al. 2013; Gershenzon et al. 2014; Huang et al. 2015) based on the seminal work of Pride (1994), who considered the electrokinetic effect and derived the governing equations for the coupled seismic and EM wave-fields in fluid-saturated porous media.

Combining the point source stacking method (Olson and Apsel 1982) and the Luco–Apsel–Chen (LAC) generalized reflection and transmission method (GRTM) (Luco and Apsel 1983; Chen 1993; Ge and Chen 2008; Ren et al. 2010a, b; Sun et al. 2019). Ren et al. (2012) developed a numerical technique to simulate seismic and EM wave-fields caused by a finite faulting in multi-layer porous media. The simulation results obtained from this numerical technique support the viewpoint that the electrokinetic effect is a possible generation mechanism of coseismic EM signals (Ren et al. 2012). The numerical technique of Ren et al. (2012) was further utilized to investigate the effect of medium structure and property on the characteristics of coseismic EM signals (Zhang et al. 2013; Huang et al. 2015). In these studies (Ren et al. 2012; Zhang et al. 2013; Huang et al. 2015), coseismic EM signals are considered just localized EM fields, which refer to the local response to relative fluid-to-solid motions induced by seismic arrivals in porous media. However, this viewpoint has been changed after the work

of Ren et al. (2016a), who identified the existence of evanescent EM waves that results from seismoelectric conversion occurring at a porous medium's interface. These seismoelectric evanescent EM waves are caused by seismic waves that arrive at a porous medium's interface with an incident angle greater than the critical angle. Their amplitudes decay rapidly when moving away from the interface. These evanescent EM waves behave as quasi-coseismic EM signals at the nearby of porous media's interfaces (Ren et al. 2016a).

The discovery of seismoelectric evanescent EM waves has attracted the interests of seismoelectric exploration researchers. Butler et al. (2018) analyzed seismoelectric experiments data obtained in Canada several years ago and consequently identified quasi-coseismic EM signals, which were interpreted by them as the evanescent EM waves predicted by Ren et al. (2016a). They pointed out that, in retrospect, evanescent EM waves had been observed in earlier seismoelectric field trials, but not recognized correctly. The recognition of seismoelectric evanescent EM waves helps explain the origin of similar effects reported in previous studies and will contribute to improved interpretation of seismoelectric records (Butler et al. 2018). In addition, evanescent EM waves can be a new form that the electrokinetic effect may take in practical application (Dietrich et al. 2018).

Numerical simulations performed by Ren et al. (2016b) show that, even for a receiver in a solid medium where the electrokinetic effect is inoperative, coseismic (or quasi-coseismic) EM signals can also be recorded because of the evanescent EM waves that originate from the seismoelectric conversion taking place at the underground water level. Therefore, coseismic EM signals can also be contributed by seismoelectric evanescent EM waves. This idea has been recently adopted by Dzieren et al. (2019). They used an equation, which was introduced by Ren et al. (2018) to describe the amplitude decay of evanescent EM waves, to quantitatively investigate the spectral ratio of seismoelectric signals that accompany seismic waves radiated from earthquake sources.

We performed a magnetotelluric (MT) survey in the Iwo-yama area of the Kirishima volcanic group (Kyushu island, Southwest Japan) to investigate its recent volcanic activities (e.g., inflation of volcanic bodies, activation in volcanic gas eruptions and development of thermal anomalies). We set up 27 MT stations around the Iwo-yama volcano, including 7 ADU07 instruments (which are produced by Metronix Company and can record two horizontal electric components, i.e., E_x and E_y , and three magnetic components, i.e., H_x , H_y and H_z) and 20 ELOG1k instruments (which are produced by NT System Design Company and can record the two

horizontal electric components, i.e., E_x and E_y). Measurements at all these MT stations started from daytime (in JST) on April 14, 2016; meanwhile the mainshock of the Kumamoto earthquake occurred at 01:25 (in JST) on April 16, 2016. The EM data were acquired until daytime (in JST) of April 28, 2016 at nearly all the stations except for 2 stations. Thus, we obtained EM signals associated with seismic waves that propagate from the Kumamoto earthquake focal areas. There also exist continuous seismic observation stations operated by ERI (Earthquake Research Institute, The University of Tokyo), JMA (Japan Meteorological Agency) and NIED (National Research Institute for Earth Science and Disaster Resilience) in the Iwo-yama area. Therefore, we can directly compare the time series of EM data with seismic signals for most earthquakes that occurred in the 2016 Kumamoto earthquake sequences. Three-dimensional (3D) inversion of the MT data obtained in the Iwo-yama area has revealed the resistivity structure, which suggests that the supply of high-temperature fluids has increased over time beneath Iwo-yama, thereby resulting in tectonic earthquakes and ground inflation (Tsukamoto et al. 2018).

In this study, we utilize the numerical technique of Ren et al. (2012) to carry out numerical simulations to explain the coseismic EM signals observed during the 2016 Kumamoto earthquakes.

Theory and method

Governing equations

Following Pride (1994), we adopt the following governing equations while the first three equations were rewritten after considering the problem to be dealt with in current study:

$$-\rho\omega^2\mathbf{u} - \rho_f\omega^2\mathbf{w} = (K_G + 4G/3)\nabla(\nabla \cdot \mathbf{u}) - G\nabla \times \nabla \times \mathbf{u} + C\nabla(\nabla \cdot \mathbf{w}) + \mathbf{F}, \quad (1)$$

$$\boldsymbol{\tau} = \mathbf{e}_z [(K_G - 2G/3)\nabla \cdot \mathbf{u} + C\nabla \cdot \mathbf{w}] + G \left[2 \frac{\partial \mathbf{u}}{\partial z} + \mathbf{e}_z \times (\nabla \times \mathbf{u}) \right], \quad (2)$$

$$-i\omega\mathbf{w} = (k_{\text{dyn}}/\eta) (-\nabla P + \rho_f\omega^2\mathbf{u} + \mathbf{f}), \quad (3)$$

$$-P = C\nabla \cdot \mathbf{u} + M\nabla \cdot \mathbf{w}, \quad (4)$$

$$\mathbf{J} = L(-\nabla P + \rho_f\omega^2\mathbf{u} + \mathbf{f}) + \sigma\mathbf{E}, \quad (5)$$

$$\nabla \times \mathbf{E} = i\omega\mu\mathbf{H}, \quad (6)$$

$$\nabla \times \mathbf{H} = -i\omega\epsilon\mathbf{E} + \mathbf{J}, \quad (7)$$

where \mathbf{u} is the average solid displacement, \mathbf{w} the average relative fluid-to-solid displacement multiplied by porosity, ω the radial frequency, ρ the bulk density, ρ_f the fluid density, $\boldsymbol{\tau}$ the traction acting on the horizontal plane, \mathbf{e}_z the unit vector in z direction, P the pore-fluid pressure, \mathbf{F} and \mathbf{f} the applied body-force densities acting on the bulk material and fluid phases, respectively, \mathbf{E} the electric field, \mathbf{H} the magnetic field, \mathbf{J} the electric current, ϵ the electrical permittivity, μ the magnetic permeability, η the fluid viscosity, K_G the Gassmann's bulk modulus, G the shear modulus. The coefficients K_G , C and M can be related to the bulk modulus of the solid and fluid phases K_s and K_f and to that of the drained framework of the solid phase K_{fr} (Haartsen and Pride 1997).

In our numerical section, dynamic permeability k_{dyn} , electrokinetic coupling coefficient L and electrical conductivity σ are determined as follows (cf. Haartsen and Pride 1997; Pride et al. 2004):

$$k_{\text{dyn}} = k_0 / \left\{ \left[1 - i\omega / (2\omega_t) \right]^{1/2} - i\omega / \omega_t \right\}, \quad (8)$$

$$L = - \left[1 - 2i(\omega / \omega_t) \right]^{-1/2} (\epsilon_0 \kappa_f \zeta) / (\eta F_f), \quad (9)$$

$$\sigma = 6.022 \times 10^{26} C_0 e^2 (1/R_{\text{Na}} + 1/R_{\text{Cl}}) / (6\pi \eta F_f), \quad (10)$$

where k_0 is the static permeability, ϵ_0 is the electrical permittivity of vacuum; κ_f is the fluid permittivity; $e = 1.6 \times 10^{-19}$ C is the fundamental charge; $R_{\text{Na}} = 1.83 \times 10^{-10}$ m and $R_{\text{Cl}} = 1.20 \times 10^{-10}$ m are the radii of ions that migrate spheres for a NaCl electrolyte. The formation factor F_f is determined by tortuosity α_∞ and porosity ϕ as $F_f = \alpha_\infty / \phi$. The transition frequency ω_t that separates the low-frequency viscous flow behavior from the high-frequency inertial flow is defined as $\omega_t = \eta / (\rho_f k_0 F_f)$. The zeta potential ζ is related to salinity C_0 as $\zeta = 0.008 + 0.026 \log_{10}(C_0)$ (Pride and Morgan 1991).

The first three terms in the right of Eq. (1) are rewritten from the term $\nabla \cdot \boldsymbol{\Gamma}$, where $\boldsymbol{\Gamma} = [K_G \nabla \cdot \mathbf{u} + C \nabla \cdot \mathbf{w}] \mathbf{I} + G [\nabla \mathbf{u} + \nabla \mathbf{u}^T - 2/3 (\nabla \cdot \mathbf{u}) \mathbf{I}]$ is the bulk stress tensor that acts on both fluid and solid phases of the porous materials. Equation (2) is just rewritten on the basis of the aforementioned bulk stress tensor by considering the relation $\boldsymbol{\tau} = \boldsymbol{\Gamma} \cdot \mathbf{e}_z$. For the adopted layered model with horizontal flat interfaces, the traction that acts on a horizontal interface $\boldsymbol{\tau}$ should be continuous when across the interface.

The original form of Eq. (3) is (Pride 1994):

$$-i\omega\mathbf{w} = (k_{\text{dyn}}/\eta) \left(-\nabla P + \rho_f \omega^2 \mathbf{u} + \mathbf{f} \right) + L\mathbf{E}. \quad (11)$$

For seismoelectric conversions where EM fields are induced by seismic waves, the term $L\mathbf{E}$ in the right-hand side of the above equation indicates the electro-osmotic feedback, by which the generated electric field acts on the electric double layers in the pores. As pointed out by Haines and Pride (2006), this electro-osmotic feedback can be neglected. The influence of this feedback can be estimated by considering the electric field caused by a compressional wave that propagates in a homogeneous porous medium. In this case, the conduction current just balances the streaming current so that $\mathbf{J}=0$. As such, Eqs. (5) and (11) yield

$$-i\omega\mathbf{w} = (k_{\text{dyn}}/\eta) \left[1 - \eta L^2 / (k_{\text{dyn}}\sigma) \right] \left(-\nabla P + \rho_f \omega^2 \mathbf{u} + \mathbf{f} \right), \quad (12)$$

where the term $\eta L^2 / (k_{\text{dyn}}\sigma)$ represents the electro-osmotic feedback and, for the material of interest, will typically satisfy $\eta L^2 / (k_{\text{dyn}}\sigma) < 10^{-5}$, which can be safely neglected relative to one. This fact allows the poroelastic wave-fields to be completely decoupled from induced EM fields (Haines and Pride 2006).

For seismoelectric conversion in fluid-saturated porous media, there are four kinds of waves, i.e., fast P wave, slow P wave, S wave and EM wave. Pride and Haartsen (1996) derived the slownesses of these waves in consideration of the electro-osmotic feedback. Following them, we obtain the wave slownesses for the present case, where the electro-osmotic feedback is neglected. The fast P wave slowness s_{pf} and slow P wave slowness s_{ps} satisfy

$$2s_{\text{pf,ps}}^2 = \chi \mp \sqrt{\chi^2 - 4(\tilde{\rho}\rho - \rho_f^2) / (HM - C^2)}, \quad (13)$$

where the minus “−” corresponds to the fast P wave, and the plus “+” corresponds to the slow P wave. Furthermore, $H = K_G + 4G/3$, $\tilde{\rho} = i\eta / (\omega k_{\text{dyn}})$ and

$$\chi = (\rho M + \tilde{\rho}H - 2\rho_f C) / (HM - C^2). \quad (14)$$

The S wave slowness s_s is given by

$$s_s = \sqrt{(\rho - \rho_f^2 / \tilde{\rho}) / G}, \quad (15)$$

and the EM wave slowness s_{em} is given by

$$s_{\text{em}} = \sqrt{\mu(\varepsilon + i\sigma / \omega)}. \quad (16)$$

However, the quality factor of fast P wave or S wave, which is determined by $Q_{\text{pf,s}} = \text{Re}(s_{\text{pf,s}}) / [2\text{Im}(s_{\text{pf,s}})]$, will be too high. Taking p_{w1} material (Table 1) as an

Table 1 Properties of the used water-saturated porous materials

Properties	p_{w1}	p_{w2}
Porosity ϕ (%)	15	45
Solid density ρ_s (10^3 kg/m^3)	2.75	2.7
Static permeability k_0 (10^{-12} m^2)	1.0	10.0
Solid bulk modulus K_s (GPa)	60.0	8.0
Frame bulk modulus K_{fr} (GPa)	34.0	5.0
Shear modulus G (GPa)	22.0	2.5
Fluid viscosity η (10^{-3} Pa s)	0.2	0.4
Salinity C_0 (10^{-3} mol/L)	5	2
Tortuosity α_∞	2	1.5
Bulk conductivity σ (S/m)	0.042	0.017
Fast P wave quality factor Q_{pf}	320	160
S wave quality factor Q_s	240	120

Parameters such as fluid density $\rho_f = 1.0 \times 10^3 \text{ kg/m}^3$, fluid bulk modulus $K_f = 2.2 \text{ GPa}$, fluid permittivity $\kappa_f = 80$ and solid permittivity $\kappa_s = 4$ are used for all water-saturated porous materials

example, if a frequency range of $f < 16 \text{ Hz}$ is considered, then Eqs. (13) and (15) will result in $Q_{\text{pf}} > 8000$ and $Q_s > 4900$, respectively. Such high-quality factors can hardly exist in the real earth (Press 1964). Therefore, in our numerical simulations, we consider Q_{pf} and Q_s as input parameters and calculate the slownesses of fast P wave and S wave by using approximation formulas as follows:

$$s_{\text{pf}} = \sqrt{\rho / H} [1 + i / (2Q_{\text{pf}})], \quad (17)$$

$$s_s = \sqrt{\rho / G} [1 + i / (2Q_s)]. \quad (18)$$

In our numerical section, referring to the observation over seismic wave attenuation in the earth crust (Press 1964), we set the quality factors Q_{pf} and Q_s ranging from about several tens to several hundreds. In addition, we calculate the slowness of slow P wave by using an approximation formula as follows:

$$s_{\text{ps}} = \sqrt{\tilde{\rho}H / (HM - C^2)}. \quad (19)$$

Numerical simulation method

Layered porous models with horizontal interfaces are used in our numerical section. Each layer is made up of a fluid-saturated (e.g., water-saturated or air-saturated) porous medium. Reflectivity methods, such as the Kennett GRTM (Kennett and Kerry 1979; Kennett 1983; Garambois and Dietrich 2002) or the LAC GRTM (Luco and Apsel 1983; Chen 1993; Ren et al. 2010b, 2012, 2016a, b; Huang et al. 2015), are effective tools for

solving wave-fields in a layered model. Martin and Thomson (1997) compared the Kennett GRTM with the LAC GRTM in detail. They observed that, the LAC GRTM is likely the key to computing the inverse of the downward transmission coefficient matrix in an unconditionally stable manner, probably because it provided more significant figures than the Kennett GRTM (Martin and Thomson 1997). The LAC GRTM has been extended to the numerical simulation of seismic waves in layered models with irregular interfaces (Chen 2007; Ge and Chen 2008). Ren et al. (2012) utilized the LAC GRTM to develop a numerical technique for simulating the propagation of electrokinetically coupled seismic and EM wave-fields in layered porous models. This numerical technique is adopted in the current work. For reader's convenience, a brief description of this numerical technique is summarized in Appendix A.

Field observation

Among the seismic stations and 27 MT stations operating in Iwo-yama area during the 2016 Kumamoto earthquakes, the MT station IWO050 was located close to the seismic station KVO with a distance of less than 1 km. These two stations can be approximately considered as one receiver with a location of (31.9443°N, 130.8483°E). This location is marked as a red triangle in Fig. 1. At the MT station IWO050, we used Pb–PbCl₂ electrodes for electric field measurement and MFS07 coils for three-component magnetic field measurement. Sampling rate was 32 Hz from 9:00 JST to 8:50 JST on the next day, and 1024 Hz in the midnight from 2:00 JST to 3:00 JST. At the seismic station KVO, three-component broadband velocity field was measured by using Trillium 120PA (Nanometrics). Sampling rate for seismic records was continuously 100 Hz.

The mainshock of the Kumamoto earthquakes was a *M*7.3 earthquake with a focal depth of 12.45 km. Its epicenter was located at (32.7545°N, 130.7630°E). Its strike, dip and rake angles were 226.1°, 71.5° and –157.9° (according to the Focal Mechanism Catalog provided by NIED). Coseismic EM signals were clearly observed for the mainshock. However, the seismic data were saturated. We selected a *M*5.4 aftershock that occurred at 01:44 (in JST) on April 16, 2016 (i.e., 19 min after the mainshock) as our research target because its hypocenter was most close to the mainshock among all the *M*5-class aftershocks. The observation results of this aftershock (Fig. 2) have remarkable data integrity and a high signal-to-noise ratio. The epicenter of this aftershock was located at (32.7532°N, 130.7615°E), and its focal depth is 15.16 km. The location of this aftershock's epicenter is marked as a red pentagram in Fig. 1. The north, east and

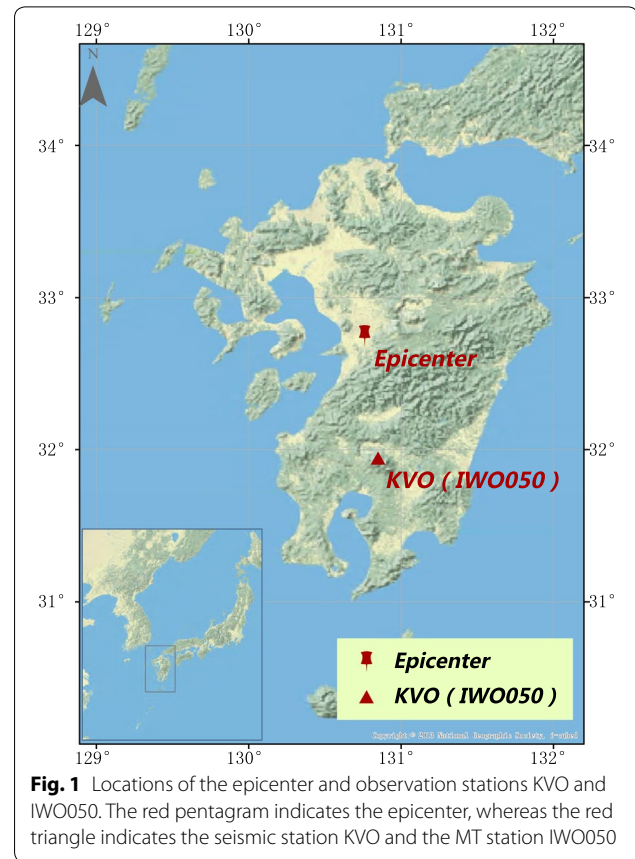


Fig. 1 Locations of the epicenter and observation stations KVO and IWO050. The red pentagram indicates the epicenter, whereas the red triangle indicates the seismic station KVO and the MT station IWO050

vertically downward directions are chosen to be the *x*-, *y*- and *z*-directions, respectively.

To obtain the seismic data commensurate with the EM data, seismic records were resampled at 32 Hz after taking an anti-aliasing digital filter. Thus, the corresponding Nyquist frequency was 16 Hz. Figure 2a displays the obtained 32 Hz data of ground vibration velocity (v_x , v_y and v_z), electric field (E_x and E_y) and magnetic induction intensity (B_x , B_y and B_z) in Cartesian coordinates while Fig. 2b displays the observed data in cylindrical coordinates (v_r , v_θ , v_z , E_r , E_θ , B_r , B_θ and B_z). In either the Cartesian coordinates or the cylindrical coordinates, the records indicate that coseismic EM signals existed for the whole duration time of seismic waves. The coseismic EM signals start to show up from the arrival time of P wave for all components of either electric or magnetic fields. Actually, coseismic EM signals associated with some previous natural earthquakes, like 1998 San Juan Bautista earthquake (Karakelian et al. 2002b), 1999 Hector Mine earthquake (Karakelian et al. 2002a), 2004 Parkfield earthquake (Gao et al. 2016), 2008 Wenchuan earthquake (Tang et al. 2010) and some earthquakes in Japan (Nagao et al. 2000), have already exhibited such a characteristic

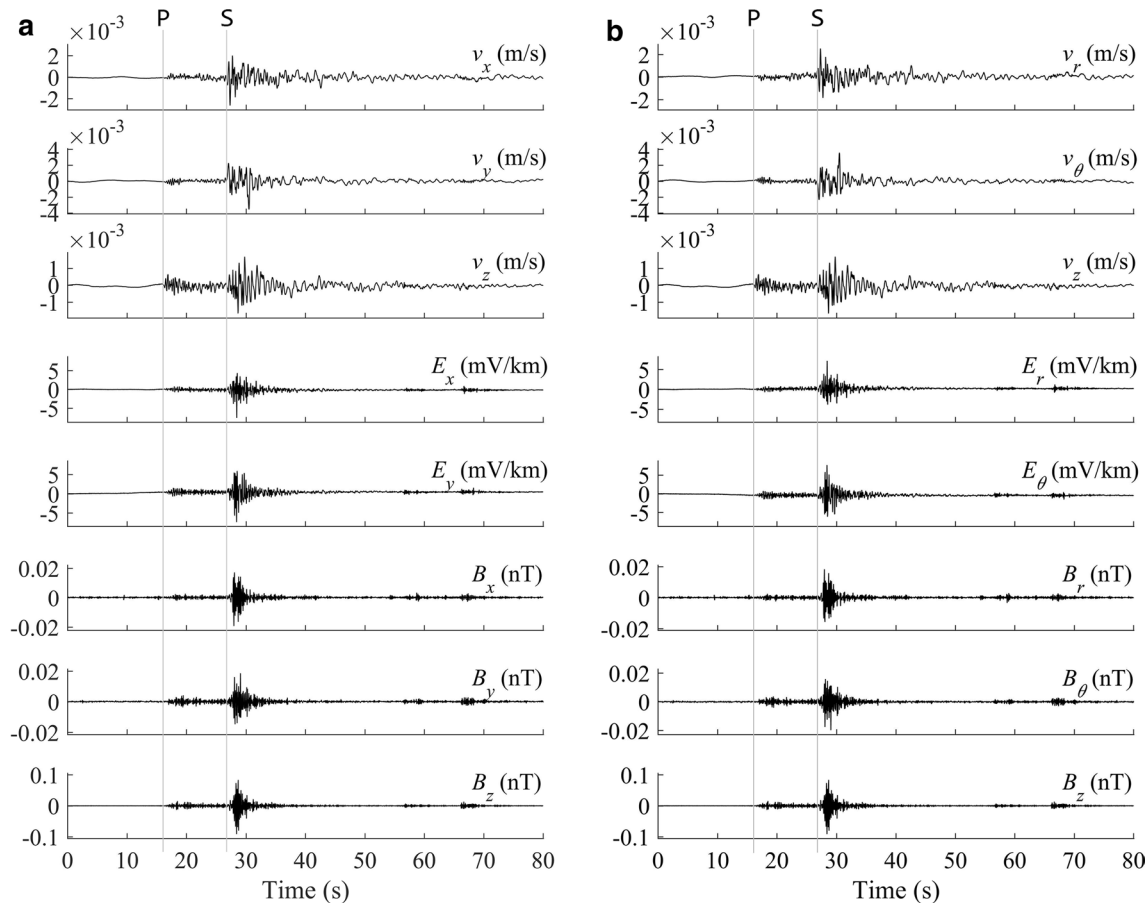


Fig. 2 Seismic and EM recordings of an aftershock. This is a $M5.4$ aftershock occurring at 01:44 (in JST) on April 16, 2016, that is, 19 min after the mainshock of $M7.3$ Kumamoto earthquake. The recordings are displayed in **a** Cartesian and **b** cylindrical coordinates, respectively. The seismic and EM time series in this figure are displayed at 32 Hz sampling rate. Thus, the frequency band of the recordings is 0–16 Hz

of showing up from the P arrival. This characteristic was also found on the coseismic EM data recorded during other aftershocks of 2016 Kumamoto earthquake. Therefore, on the basis of field observational results, we can conclude this is a commonly observed characteristic for coseismic EM signals in the real case.

A specialness for these observation data is that the MT station IWO050 and the seismic station KVO were located at nearly the due south of the epicenter. Therefore, the x - and y -components are nearly equivalent to the r - and θ -components, respectively, except that their amplitudes have a difference of minus sign. Figure 2b shows that, for the seismic signals recorded before the S arrival, the maximum amplitude of the v_θ component is comparable with or probably greater than that of the v_r component. We can also see the maximum amplitudes of E_r and B_r components are generally comparable with those of E_θ and B_θ components, respectively. Previous studies on coseismic EM signals from either field observation (Nagao et al. 2000; Karakelian et al. 2002a, b; Matsushima et al. 2002;

Tang et al. 2010; Gao et al. 2016) or numerical simulation aspects (Hu and Gao 2011; Ren et al. 2012, 2015, 2016a, b; Zhang et al. 2013; Huang et al. 2015; Gao et al. 2016) have used Cartesian coordinates only. Simulation and observation results have never been compared in cylindrical coordinates. In this work, we perform such kind of comparison.

Models based on previous electrokinetic studies

To explain the observation results displayed in Fig. 2, we adopt several models based on previous electrokinetic studies and perform numerical simulations. Unfortunately, none of these models can explain the observed coseismic EM signals well, especially the recorded magnetic signals before the S arrival.

In our numerical simulations, the following configurations are adopted for all used models. The epicenter of the $M5.4$ aftershock is chosen to be the coordinate origin. We approximately take the distance of 1° as 100 km, and the bird view of the epicenter and receiver is set as shown in Fig. 3a. This aftershock is not a great earthquake and

the epicentral distance is greater than 80 km, which is long enough. Therefore, we consider the fault as a double-couple point source. The moment released by the double-couple point source is assumed to be equal to that released by a fault with an area of $3 \times 2 \text{ km}^2$ and an averaged final slip displacement of 0.96 m. The focal depth is set as 15.16 km. The focal mechanism of this aftershock is unknown. However, since this aftershock occurred only 19 min after the mainshock and the aftershock epicenter was very close to the mainshock epicenter (the distance was about 200 m), it is generally reasonable to assume the

focal mechanism of this aftershock is close to that of the mainshock. Therefore, referring to the focal mechanism of the mainshock, we set the strike, dip and rake angles of this aftershock as 234° , 72° and -117° . The applied source time function is a Bouchon's ramp function with shift, which can be written as

$$Ra(t) = 0.5 + 0.5 \cdot \tanh \left[(t - t_{\text{shift}}) / t_{\text{arise}} \right], \quad (20)$$

where t_{shift} and t_{arise} are the time shift and the arise time, respectively. They are set as $t_{\text{shift}} = 1.3 \text{ s}$ and $t_{\text{arise}} = 0.45 \text{ s}$

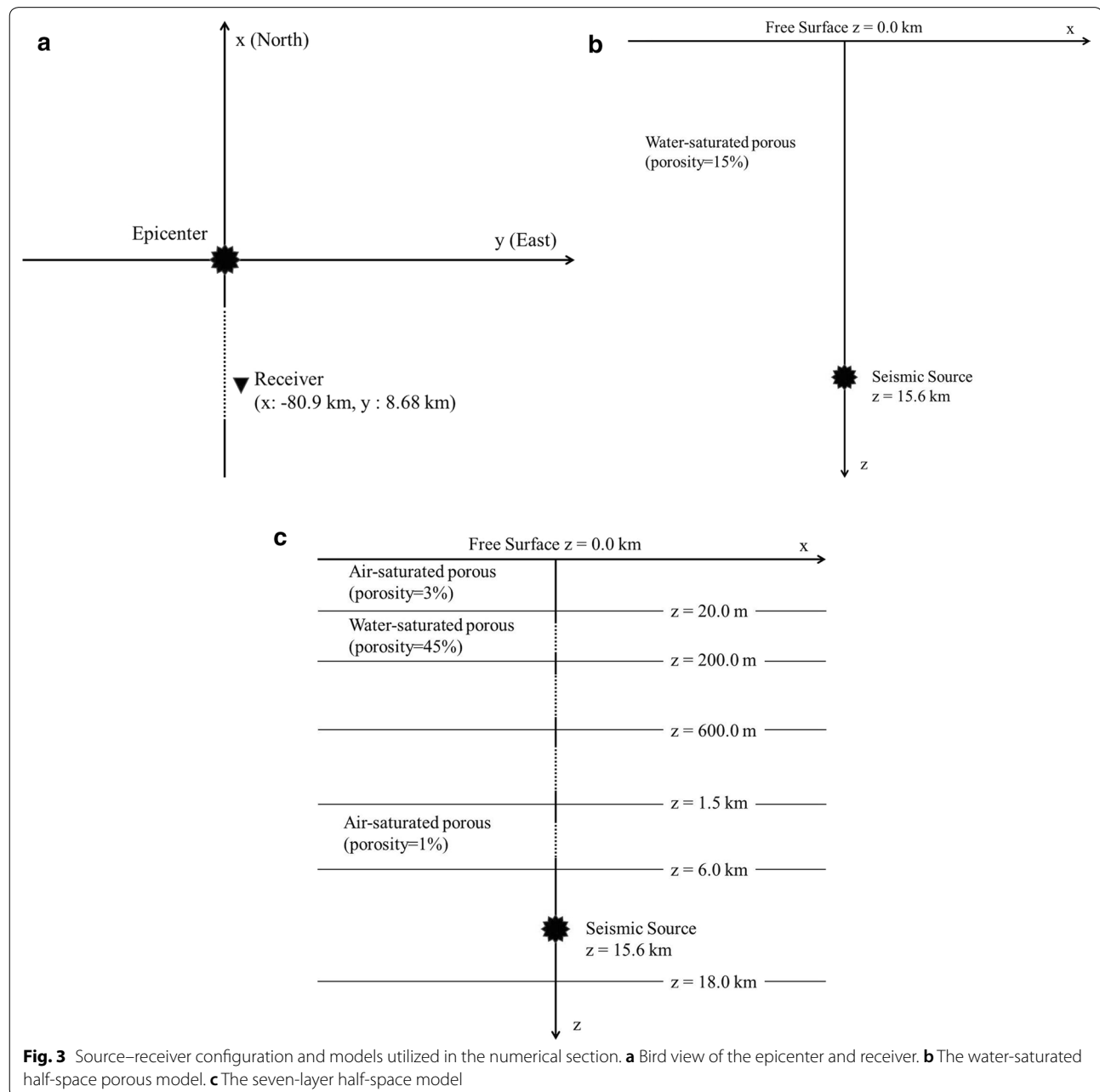


Fig. 3 Source-receiver configuration and models utilized in the numerical section. **a** Bird view of the epicenter and receiver. **b** The water-saturated half-space porous model. **c** The seven-layer half-space model

in our numerical simulations. The seismic and EM wave-fields are calculated for the frequency range of $0 \leq f \leq 16$ Hz.

Water-saturated half-space porous model

In the last several years, some numerical simulation studies on coseismic EM signals (Hu and Gao 2011; Ren et al. 2012, 2015; Zhang et al. 2013; Huang et al. 2015; Gao et al. 2016) have utilized the multilayer water-saturated half-space models. A trend that such model is typical and correct for the modeling of coseismic EM signals seems to exist. Therefore, we first consider a basic representative of such model, that is, a water-saturated half-space porous model (Fig. 3b) that consists of material p_{w1} ; the properties of this model can be found in Table 1. The released moment is 1.27×10^{17} N m given that the shear modulus of the p_{w1} material is 22.0 GPa.

We first consider a receiver with a depth of 0.1 m, which is an ordinary case in field observation. Figure 4a

shows the multiple components of the simulated seismic and EM wave-fields. Three components of ground vibration velocity (v_x , v_y and v_z), two horizontal components of electric field (E_x and E_y) and three components of magnetic induction intensity (B_x , B_y and B_z) are displayed. The SV wave that arrives at the ground surface with a critical angle of $\theta_{\text{ref}} = \arcsin(V_s/V_{\text{pf}})$, where V_s and V_{pf} indicate the velocities of S and fast P waves, will generate converted P wave that propagates along the ground surface. This wave is the so-called refracted SV–P wave. It will show up after the P arrival but before the S arrival when the epicentral distance is sufficiently long. In addition, the Rayleigh wave whose velocity is slightly slower than the S wave velocity will develop well at a sufficiently long epicentral distance. Therefore, in Fig. 4a, the arrivals of P, refracted SV–P, S and Rayleigh waves are evident on the seismogram (v_x , v_y and v_z). These arrivals can also be found on the electrogram (E_x and E_y). However, only the S arrival can be seen on the magnetogram (B_x , B_y and

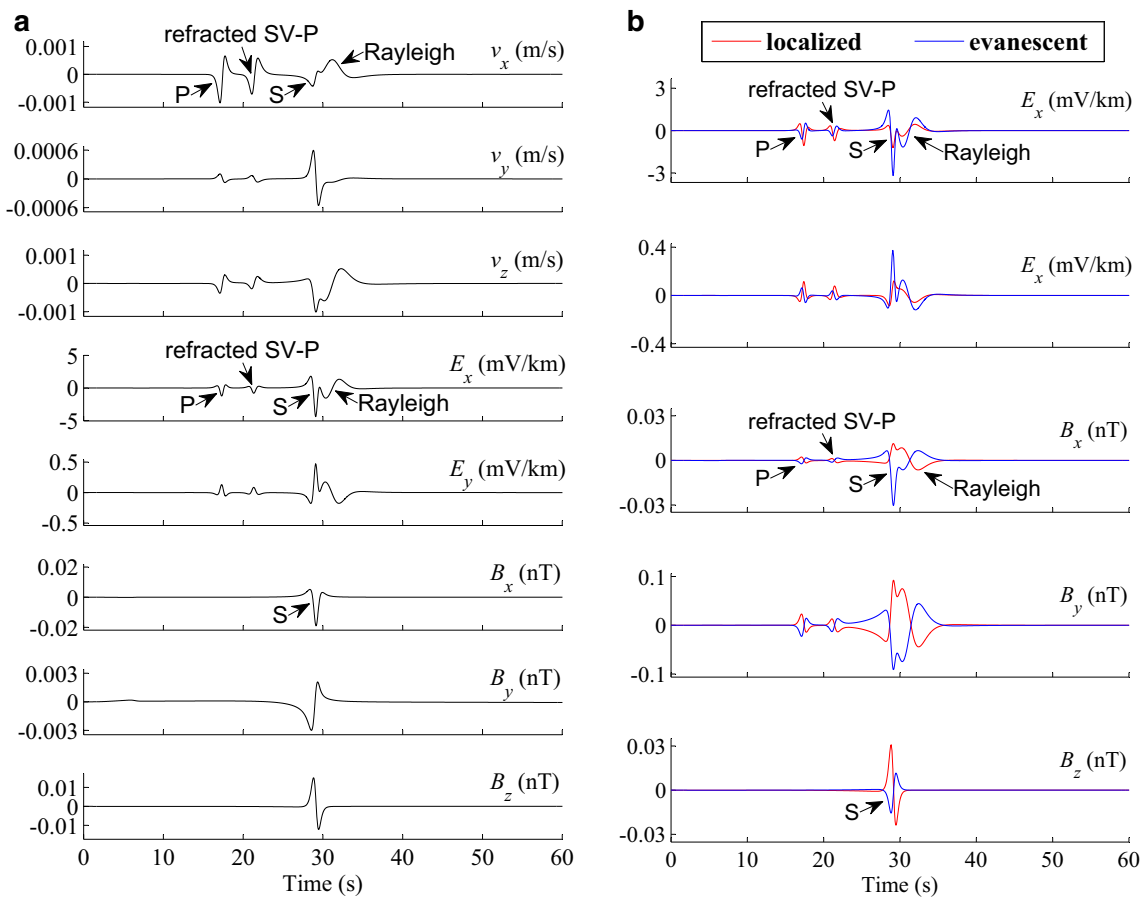


Fig. 4 Seismic and EM signals simulated for the water-saturated half-space porous model. Multiple components of **a** seismic and EM wave-fields and **b** localized and evanescent EM waves are calculated for a receiver nearby the ground surface, which is located at (−80,890, 8680, 0.1) m

B_z). Thus, the showing up time of the coseismic magnetic signals is an evident difference between the simulation result (Fig. 4a) and the observation result (Fig. 2a). Furthermore, some weak signals show up around 3–7 s in the B_y component. These signals are interfacial radiation EM waves induced by nearly normal incidence of seismic waves on the porous media's interface, that is, the free surface of this water-saturated half-space model. Such kind of interfacial radiation EM waves have been confirmed in both numerical simulation (e.g., Haartsen and Pride 1997; Garambois and Dietrich 2002) and field experiment studies (e.g., Butler et al. 2018).

For the present case where the receiver is nearly located at the due south of the epicenter (Fig. 3a), the x - and y -components are very close to the r - and θ -components, respectively, except that the amplitudes have a difference of minus sign. Theoretically, v_r component records P and SV waves, whereas v_θ component records SH wave for a layered model with horizontal interface(s). Apparently, SH wave does not show up before the S arrival because P wave can generate converted P–P and P–SV waves but not converted P–SH wave. Therefore, before the S arrival, v_y component, which is close to v_θ component, has evidently weaker signal strength than v_x component, which is close to v_r component. In addition, the maximum amplitudes of E_x and B_x components are evidently greater than those of E_y and B_y components (Fig. 4a). Comparing Fig. 4a with Fig. 2a, we find another difference, that is, the maximum amplitude ratios of v_x to v_y (for those before the S arrival), E_x to E_y and B_x to B_y obtained from the simulation result (Fig. 4a) are several times greater than those obtained from the observation result (Fig. 2a).

As pointed out by Ren et al. (2016a), evanescent EM waves can be generated by seismoelectric conversion at a vacuum-porous interface as which the ground surface of the water-saturated half-space porous model can be considered. According to some theoretical and numerical simulation studies (Pride and Haartsen 1996; Haartsen and Pride 1997; Ren et al. 2016a, b, 2018), the simulated coseismic EM signals shown in Fig. 4a are contributed by two parts, namely, the localized EM fields that are characterized by seismic wave velocities and the evanescent EM waves with phase velocity of EM velocity. These two parts are separately calculated and shown in Fig. 4b. The vertical magnetic component theoretically can only be induced by SH wave when a horizontally layered model is used (Ren et al. 2015). Therefore, the localized and evanescent EM signals only show up for S arrival on B_z component (Fig. 4b). However, on E_x , E_y , B_x and B_y components, the signals that seemingly accompany P, refracted SV–P, S and Rayleigh waves exist for either the localized or evanescent EM signals. For some parts, the horizontal magnetic signals (B_x and B_y) seemingly

accompany P, refracted SV–P and Rayleigh waves, and the localized EM signals are just counterbalanced by the evanescent EM signals. In sum, the magnetic signals only show up at the S arrival in the total fields of B_x , B_y and B_z components (Fig. 4a).

Still adopting the water-saturated half-space porous model, we calculate the seismic and EM wave-fields for receivers with the same lateral offsets but different depths. The lateral offsets are still set as $x_r = -80,890$ m and $y_r = 8680$ m, and 4 receivers with depths $z_r = 0, 500, 1000$ and 1500 m are considered. The simulation result is shown in Fig. 5. B_x signals shown in the gray box are amplified by a factor of 7 to improve the visibility. The seismic and EM wave-fields calculated for the receiver with the depth of $z_r = 0$ m (red lines in Fig. 5) are almost the same as those calculated for the receiver with the depth of $z_r = 0.1$ m (Fig. 4a). The red lines indicate that no magnetic signal shows up before the S arrival. As the receiver depth increases, the waveforms and amplitudes of seismic and EM wave-fields are more or less changed. One significant change is that B_x and B_y signals begin to show up at the arrivals of P, refracted SV–P and Rayleigh waves. The strengths of these magnetic signals generally become stronger for deeper receiver.

Figure 6 shows the localized EM fields and evanescent EM waves simulated for the four above-mentioned receivers with different depths. The signals in the gray boxes are amplified to have a better visibility. Theoretically, the localized electric field accompanies both P and S waves, whereas the localized magnetic field only accompanies S waves (Pride and Haartsen 1996). In Fig. 6a, the localized B_x and B_y signals before the S arrival actually are generated by the converted P–SV and refracted SV–P–SV waves. The strengths of these magnetic signals do not have significant variation. For a deeper receiver, the converted P–SV and refracted SV–P–SV waves arrive later. Therefore, the corresponding localized magnetic signals (i.e., the localized B_x and B_y signals before the S arrival) show evident delay of arrival time (Fig. 6a).

The evanescent EM waves are induced by seismic waves that arrive at the ground surface with an incident angle greater than a critical angle

$$\theta_{\text{eva}} = \arcsin(V_{\text{sei}}/V_{\text{em}}),$$

where V_{sei} and V_{em} represent the seismic and EM velocities, respectively. The arrival time of the evanescent EM waves is the same as that of seismic waves at the normal projection point of the receiver onto the ground surface. The normal projection points onto the ground surface of the four receivers are identical at (80,890, 8680, 0) m, because they have the same lateral offsets. Therefore, the arrival time of the evanescent EM waves shows no variation for the four different receivers (Fig. 6b). One

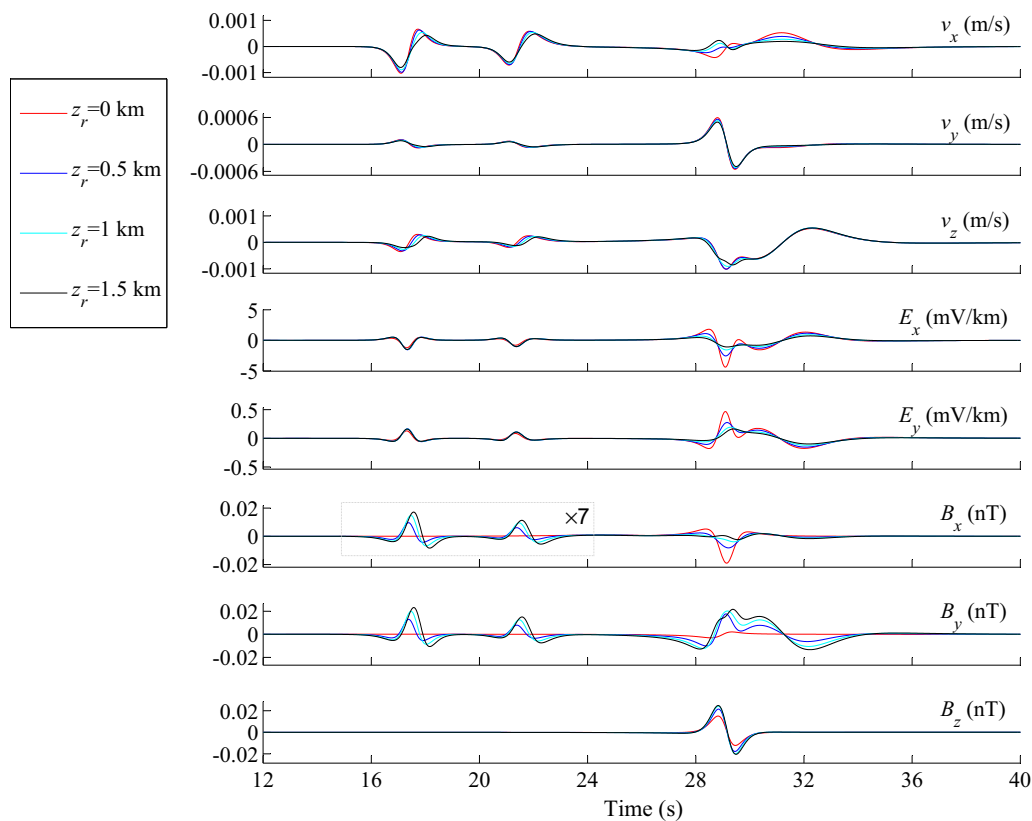


Fig. 5 Seismic and EM signals calculated for four different receivers in the water-saturated half-space porous model. These four receivers have different depths $z_r=0, 500, 1000$ and 1500 m but the same lateral offset $x_r=-80,890$ m and $y_r=8680$ m. B_x signals in the gray box are amplified by a factor of 7 to improve the visibility

significant characteristic of the evanescent EM waves is the amplitude decay when moving away from the interface. Figure 6b shows this characteristic clearly. The amplitudes of the evanescent EM waves dramatically decrease for deeper receiver. For receivers at the depths of $z_r=500, 1000$, and 1500 m, the localized magnetic signals that accompany the converted P-SV, refracted SV-P-SV and Rayleigh waves are no longer counterbalanced by the corresponding evanescent EM waves. Therefore, the total B_x and B_y components show signals that seemingly accompany all seismic wave types for receivers at depths (see blue, cyan and black lines in Fig. 5).

We also test several multilayer water-saturated half-space models. The waveforms of seismic and EM wavefields are more complicated because of the multiple reflections that occur on the interfaces. However, the magnetic signals before the S arrival are still invisible for the receiver located at or nearby the ground surface.

In field observations, the EM observation equipment is usually placed nearby the ground surface; for example, at depth less than 1 m. The observed coseismic magnetic signals always show up in the whole seismic arrival time

domain (Honkura et al. 2000; Karakelian et al. 2002a, b; Tang et al. 2010; Matsushima et al. 2013; Tsutsui 2014). Thus, the behavior of the numerically simulated magnetic signals is evidently different from the field observations. This problem was first discussed by Ren et al. (2015). However, at that time, Ren et al. (2015) did not realize the existence of evanescent EM waves resulting from the seismoelectric conversion occurring at an interface of a porous medium (Ren et al. 2016a). Hence, Ren et al. (2015) did not know that the evanescent EM waves play an important role nearby the ground surface of the water-saturated half-space model. They finally proposed a surface-charge assumption that could enable the simulated horizontal magnetic signals to show up at all seismic arrivals (Ren et al. 2015). However, Ren et al. (2015) only investigated this problem in Cartesian coordinates, and the surface-charge assumption could not improve the behavior of the simulated vertical magnetic component that shows up at only the S arrival. The surface-charge assumption (Ren et al. 2015) will be further investigated in the following context.

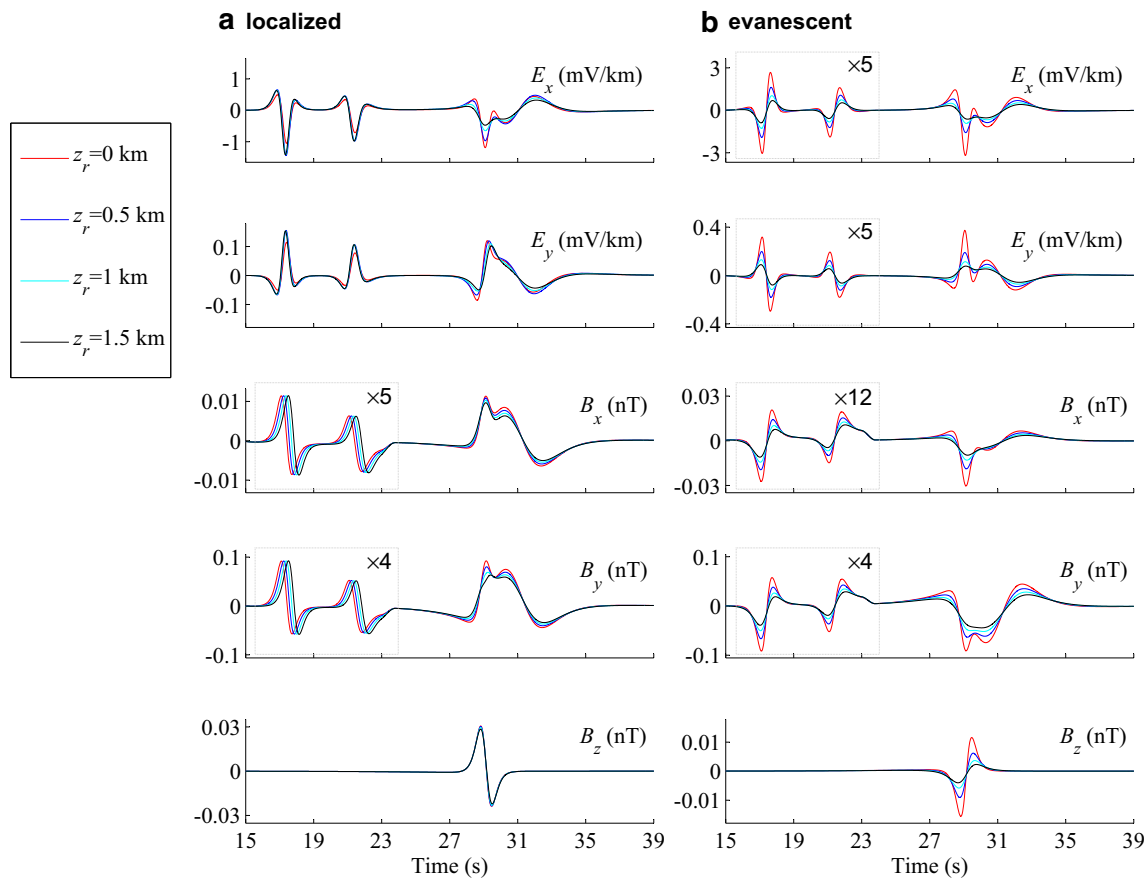


Fig. 6 Comparison between **a** localized EM fields and **b** evanescent EM waves. These wave-fields are calculated for the four receivers with the same lateral offset $x_r = -80,890$ m and $y_r = 8680$ m, but different depths $z_r = 0, 500, 1000$ and 1500 m in the water-saturated half-space porous model. The signals in the gray boxes are amplified to have a better visibility

Layered model consisting of porous media saturated by air or water

Ren et al. (2016b) conducted numerical simulations by adopting an eight-layer half-space model consisting of porous and solid materials; they found that coseismic EM signals can also be recorded by a receiver located in the top solid layer, where the electrokinetic effect is inoperative. In this case, the coseismic EM signals are contributed by the evanescent EM waves. It is different from the case of water-saturated half-space porous model, where the coseismic EM signals recorded nearby the ground surface are contributed by both the localized EM fields and the evanescent EM waves.

The multilayer water-saturated half-space models used in some previous numerical simulations of coseismic EM signals (Hu and Gao 2011; Ren et al. 2012, 2015; Zhang et al. 2013; Huang et al. 2015; Gao et al. 2016) may not fit the real case. For example, the water table is usually located underground, and the aquifer often has a finite thickness. The aquifer can be considered a

water-saturated porous medium. The media above and below the aquifer probably can be treated as air-saturated porous medium. The upper medium presumably has a relatively higher porosity to allow water to pass through, whereas the lower medium likely has a relatively lower porosity to avoid infiltration. Considering the above-mentioned reason and referring to the model utilized by Ren et al. (2016b) and the conductivity (resistivity) structure obtained by Tsukamoto et al. (2018), we consider a seven-layer half-space model that consists of porous media saturated by water or air. This seven-layer half-space model is a conceptual model, and its configuration is shown in Fig. 3c. To facilitate the analysis conducted in the following context, we consider only one aquifer, that is, the second layer between the depths of 20 and 200 m. It consists of water-saturated porous material p_{w2} whose properties are listed in Table 1. The six other layers are made up of air-saturated porous materials p_{a1} , p_{a2} , p_{a3} , p_{a4} , p_{a5} and p_{a6} , whose properties are listed in Table 2. For these air-saturated porous materials, the electrokinetic

coupling coefficient is assumed to be $L=0$. Given that p_{a5} material, where the source is located, has a shear modulus of 27.0 GPa, the released moment is 1.56×10^{17} N m. We again consider a receiver located at $(-80,890, 8680, 0.1)$ m.

Figure 7 shows the simulated seismic and EM wavefields. Nonetheless, no magnetic signal shows up during the time period between P and S arrivals. Since the conductivity of earth media has a large range of variation, we also conduct numerical simulations for the seven-layer half-space model by setting different conductivity values that range from 10^{-4} to 0.1 S/m, which are presumably possible for the shallow earth crust. It is always found there is no visible magnetic signal during the time period between P and S arrivals. Therefore, if only the electrokinetic effect is considered, the simulation result of the seven-layer half-space model consisting of water-saturated and air-saturated porous materials shows evident difference from the observation result on the magnetic signals before the S arrival. In addition, the signal strengths of v_x , E_x and B_x components are several times (about 5–10 times) stronger than those of v_y , E_y and B_y components, respectively (Fig. 7). This result is evidently different from the observation result shown in Fig. 2a.

Electrokinetic effect combined with surface-charge assumption

Pride and Haartsen (1996) mentioned the possibility of the interface carrying surface-charge density Q_{sc} . They pointed out such a surface-charge density will arise because of the electrokinetic effect if a background fluid flow passes through the interface. However, such a surface-charge density is usually ignored in the numerical simulation study on the electrokinetic effect (Haartsen

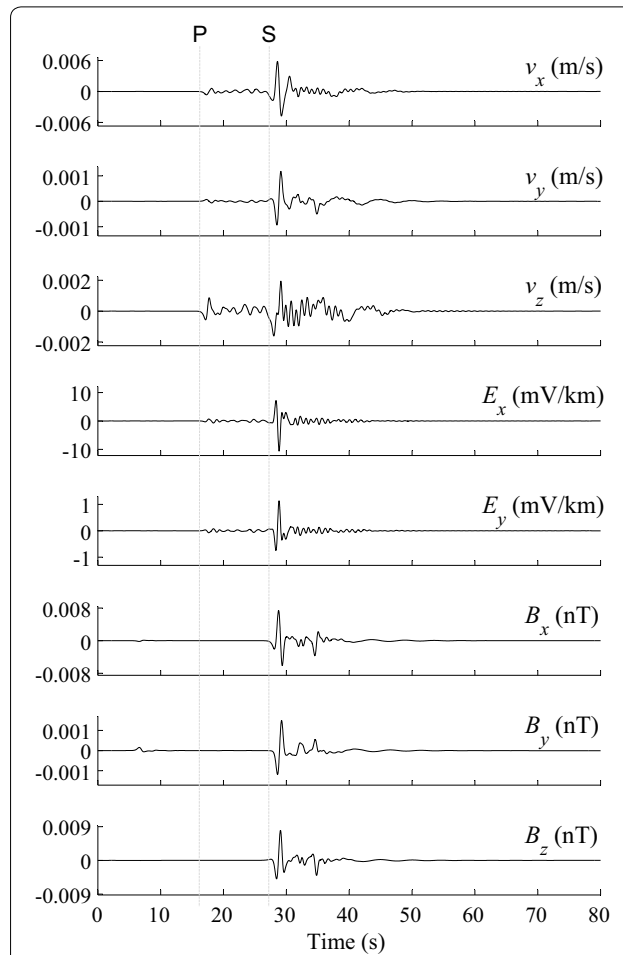


Fig. 7 Seismic and EM signals simulated for the seven-layer half-space model. The receiver is located at $(-80,890, 8680, 0.1)$ m. Neither the surface-charge assumption nor the scattering effect is considered

Table 2 Properties of the used air-saturated porous materials

Properties	P_{a1}	P_{a2}	P_{a3}	P_{a4}	P_{a5}	P_{a6}
Porosity ϕ (%)	3	1	1	1	1	1
Solid density ρ_s (10^3 kg/m ³)	2.1	2.7	2.7	2.7	2.75	2.8
Static permeability k_0 (10^{-12} m ²)	10^{-3}	10^{-4}	10^{-4}	10^{-4}	10^{-4}	10^{-4}
Solid bulk modulus K_s (GPa)	8.0	10.0	15.0	50.0	60.0	60.0
Frame bulk modulus K_{fr} (GPa)	5.6	7.0	9.0	36.0	42.0	48.0
Shear modulus G (GPa)	2.1	5.0	7.0	22.0	27.0	33.0
Air viscosity η (10^{-3} Pa s)	0.018	0.018	0.018	0.018	0.018	0.018
Tortuosity α_∞	4	8	8	8	8	8
Bulk conductivity σ (S/m)	0.01	0.01	0.01	0.01	0.01	0.0001
Fast P wave quality factor Q_{pf}	120	200	240	280	320	400
S wave quality factor Q_s	90	150	180	210	240	300

Parameters such as fluid density $\rho_f = 1.29$ kg/m³, fluid bulk modulus $K_f = 0.15$ MPa, fluid permittivity $\kappa_f = 1$ and solid permittivity $\kappa_s = 4$ are used for all air-saturated porous materials

and Pride 1997; Ren et al. 2010a, 2010b, 2012; Zhang et al. 2013; Huang et al. 2015). Ren et al. (2015) pointed out that fluid flow across the ground surface can be induced by the condensation of water vapor near the ground surface at low temperature, the evaporation of the soil water near the ground surface at high temperature, rainfall, melting snow on ground surface, or some other causes. Thus, there is a possibility that surface-charge on ground surface can be electrokinetically induced by one kind or the combination of several kinds of fluid flows (Ren et al. 2015). When seismic waves arrive at such a precharged ground surface, an effective surface current $i\omega \mathbf{n} \times \mathbf{n} \times \mathbf{u} Q_{sc}$ (where \mathbf{n} is the normal of the ground surface) will exist, thereby leading to the discontinuity of the horizontal magnetic components. As a result, additional EM waves will be generated by seismic waves arriving at a ground surface carrying surface-charge density. The detailed mathematical formulas for determining the generalized reflection coefficients at the ground surface for the case of considering surface-charge density, which is

different from the case of surface-charge density ignored, were derived by Ren et al. (2015).

Still adopting the seven-layer half-space model (Fig. 3c), we now consider the surface-charge assumption. Referring to the estimated surface-charge density Q_{sc} expected at the earth's surface (Ren et al. 2015), we set a value of $Q_{sc} = -0.02 \text{ C/m}^2$. The simulated seismic and EM wave-fields are displayed in the Cartesian coordinates (Fig. 8a) and cylindrical coordinates (Fig. 8b), respectively. Comparing Fig. 8a with Fig. 7, we find the surface-charge density does not affect the seismic signals (v_x , v_y and v_z components) but influence the coseismic EM signals. To some extent, it does help improve the simulation result because the signals before the S arrival begin to show up on B_x and B_y components (Fig. 8a). However, these signals are still missing on B_z component. Furthermore, in the simulation result displayed in cylindrical coordinates (Fig. 8b), the signals before the S arrival are missing on several components, including v_θ , E_θ , B_r and B_z components. However, in the observation result displayed

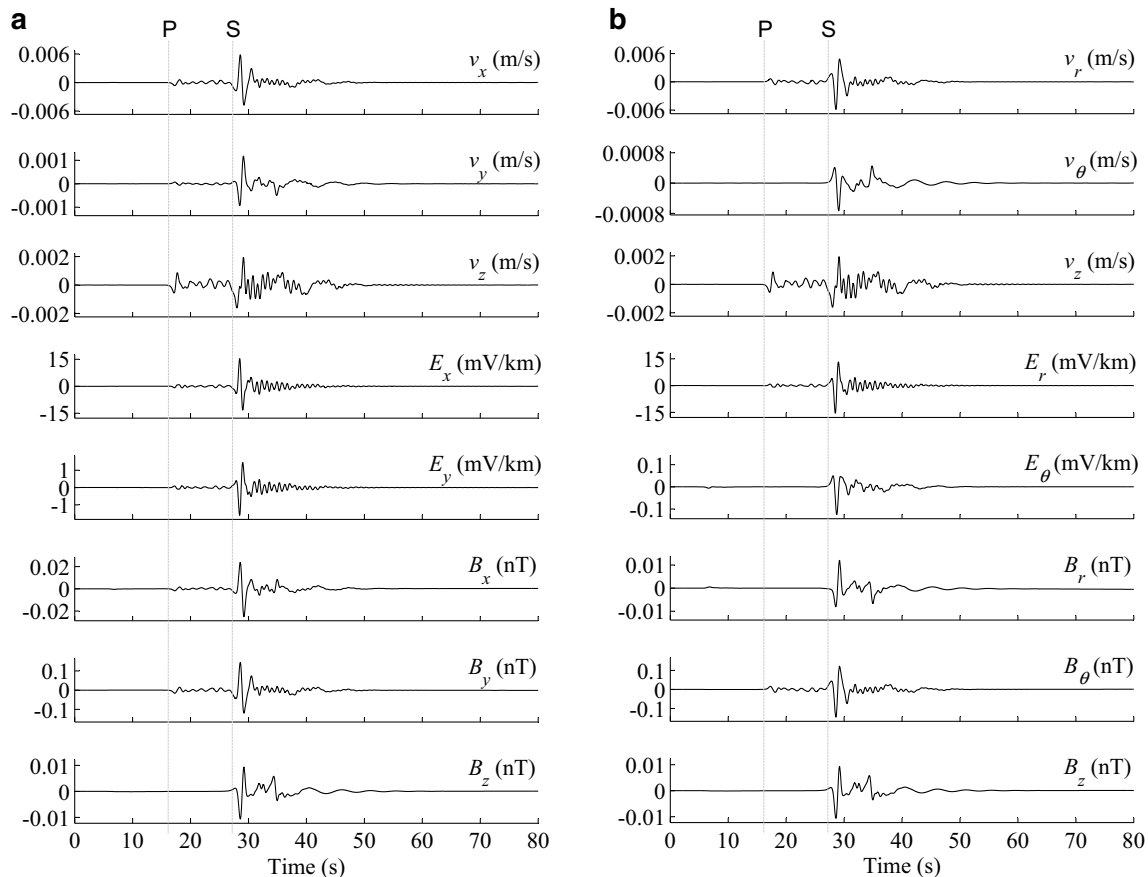


Fig. 8 Seismic and EM signals recomputed for the seven-layer half-space model. The receiver is still located at $(-80, 890, 8680, 0.1) \text{ m}$, but a surface-charge density of $Q_{sc} = -0.02 \text{ C/m}^2$ is considered. The simulated seismic and EM wave-fields are displayed in **a** Cartesian and **b** cylindrical coordinates, respectively

in cylindrical coordinates (Fig. 2b), the signals on each component of seismic, electric or magnetic fields always begin to show up from the P arrival.

Another difference from the observation result (Fig. 2) is that the signal strength ratio of x -component to y -component or r -component to θ -component is excessively large or small. The signal strengths of v_x , E_x , v_r and E_r components are much stronger than those of v_y , E_y , v_θ and E_θ components, respectively. The signal strength difference between E_r and E_θ even reaches two orders of magnitude. Compared with Fig. 7, the magnetic signals shown in Fig. 8 are dramatically enhanced. The signal strengths of B_x and B_r components are much weaker than those of B_y and B_θ components, respectively. Therefore, simulation results based on the combination of electrokinetic effect and surface-charge assumption still cannot explain the field observation well.

Electrokinetic effect combined with scattering effect

Introducing an artificial scattering effect

The simulation results in Figs. 4, 7 and 8 show that, for the signals before the S arrival, the v_x component has much stronger signal strength than the v_y component, which is theoretically reasonable for the adopted configuration of the epicenter and the receiver (Fig. 3a) when considering a layered model with horizontal interfaces. However, the situation in the observation result (Fig. 2) is different from the above situation. Given that the observation stations were located in a volcanic area, fairly strong heterogeneities of seismic velocity and strong topographic variations presumably exist. Scattering of primary seismic waves can be induced by both the localized volume heterogeneity and the irregular topography (Levander 1990). As predicted by theory and observed in the field, the influence of scattering effect on seismic waves includes attenuation, fluctuations, seismic wave-type conversions, and coda (Aki 1969, 1973, 1980; Aki and Chouet 1975; Wu 1982; Wu and Aki 1985). The seismic wave-type conversions include PSV-to-SH and SH-to-PSV conversions that produce energy on components where there would be none in a horizontally layered media. Therefore, the scattering effect probably has played an important role in generating the coseismic EM signals in the volcanic area.

To include the scattering effect naturally in the modeling of coseismic EM signals, we need to consider a 3D porous model with seismic velocity heterogeneities and a topographic free surface. For such a model, a power numerical technique that can solve both seismic and EM wave-fields is still to be developed. In the following numerical simulations, we attempt to bring in the

PSV-to-SH and SH-to-PSV conversions in a rough and simple manner, although these seismic wave-type conversions cannot take place for the used layered model with horizontal interfaces (Fig. 3c). In this manner, a fictitious scattering effect is mandatorily introduced into our simulations. Therefore, we call it artificial scattering effect. This goal is achieved by the following three steps.

First, we assume additional PSV-to-SH and SH-to-PSV conversions occur at the ground surface. The converted seismic waves act as additional sources generating additional seismic and EM wave-fields due to the multiple reflections and transmissions on the interfaces. An artificial scattering conversion coefficient C_{st} is used to connect the converted seismic waves to the original seismic waves recorded at the ground surface. Expressions using the expansion coefficients are written as

$$u_{T,m}^{\text{Converted}(0)} = C_{st} u_{S,m}^{(1)}(z^{(0)}), \quad (21)$$

$$u_{S,m}^{\text{Converted}(0)} = C_{st} u_{T,m}^{(1)}(z^{(0)}), \quad (22)$$

where $u_{T,m}^{\text{Converted}(0)}$ and $u_{S,m}^{\text{Converted}(0)}$ are the expansion coefficients of the seismic waves generated at the ground surface $z = z^{(0)} = 0$ due to the additional PSV-to-SH and SH-to-PSV conversions. The additional source term vectors $\mathbf{b}^{\text{AddedSHTE}}(z^{(0)})$ and $\mathbf{b}^{\text{AddedPSVTM}}(z^{(0)})$ corresponding to the additional PSV-to-SH and SH-to-PSV conversions satisfy

$$\Theta^{\text{SHTE}(1)}(1, :) \Lambda^{\text{SHTE}(1)}(z^{(0)}) \mathbf{b}^{\text{AddedSHTE}}(z^{(0)}) = u_{T,m}^{\text{Converted}(0)}, \quad (23)$$

$$\begin{aligned} \Theta^{\text{PSVTM}(1)}(1, :) \Lambda^{\text{PSVTM}(1)}(z^{(0)}) \mathbf{b}^{\text{AddedPSVTM}}(z^{(0)}) \\ = u_{S,m}^{\text{Converted}(0)}. \end{aligned} \quad (24)$$

Once the additional source term vectors $\mathbf{b}^{\text{AddedSHTE}}(z^{(0)})$ and $\mathbf{b}^{\text{AddedPSVTM}}(z^{(0)})$ are determined, the LAC GRTM (Luco and Apsel 1983; Chen 1993; Ren et al. 2012) can be utilized to obtain the adjusted wave-field amplitude vectors $\mathbf{a}^{\text{AddedSHTE}}$ and $\mathbf{a}^{\text{AddedPSVTM}}$, which will be substituted into Eq. (30) to determine the expansion coefficients of the additional seismic and EM wave-fields $u_{T,m}^{\text{Added}}$, $u_{S,m}^{\text{Added}}$, $u_{R,m}^{\text{Added}}$, $E_{T,m}^{\text{Added}}$, $E_{S,m}^{\text{Added}}$, $H_{T,m}^{\text{Added}}$ and $H_{S,m}^{\text{Added}}$.

Second, the original wave-fields are weakened by being multiplied with a factor of $\sqrt{1 - C_{st}^2}$. Then, they are added onto the additional wave-fields. Thereafter, the expansion coefficients of the total wave-fields are given as

$$A_{\xi,m}^{\text{Total}} = \sqrt{1 - C_{st}^2} A_{\xi,m} + A_{\xi,m}^{\text{Added}}, \quad (25)$$

where $A = u, E$ or H , and $\xi = T, S$ or R . Substitution of these expansion coefficients into Eq. (38) provides the total seismic and EM wave-fields expressed in cylindrical coordinates $A_r^{\text{Total}}, A_\theta^{\text{Total}}$ and A_z^{Total} . Equations (21)–(25) are in the frequency–wavenumber domain.

Third, in addition to the seismic waves directly from the source, there should be some contributions from other directions due to the scattering effect. This may be the reason why the observation result shows that the signal strength of v_y (or v_θ) component is comparable with or even stronger than that of v_x (or v_r) component at the part before the S arrival (Fig. 2). We roughly consider this effect by rotating the horizontal components of the total wave-fields with an angle of θ_{rot} . Thus the finally obtained wave-fields are calculated as follows:

$$\begin{cases} A_r^{\text{Final}} = A_r^{\text{Total}} \cos \theta_{\text{rot}} - A_\theta^{\text{Total}} \sin \theta_{\text{rot}} \\ A_\theta^{\text{Final}} = A_r^{\text{Total}} \sin \theta_{\text{rot}} + A_\theta^{\text{Total}} \cos \theta_{\text{rot}} \\ A_z^{\text{Final}} = A_z^{\text{Total}} \end{cases} \quad (26)$$

where $A = u, E$ or H . These wave-fields expressed in cylindrical coordinates can be easily converted into Cartesian coordinates $A_x^{\text{Final}}, A_y^{\text{Final}}$ and A_z^{Final} .

Although the scattering effect introduced in the above is artificial and special, we can utilize it to investigate the possible influence of the scattering effect on the coseismic EM signals.

New numerical simulation results

Then, numerical simulations are carried out on the seven-layer half-space model (Fig. 3c) by considering the artificial scattering effect described in the above. We test different artificial scattering conversion coefficients as well as different horizontal wave-field rotation angles.

Figure 9 shows the simulated seismic and EM wave-fields when an artificial scattering conversion coefficient $C_{\text{st}} = 0.6$ and a horizontal wave-field rotation angle of 30° in the counterclockwise direction are considered. The simulation result displayed in Cartesian coordinates (Fig. 9a) shows that the coseismic magnetic signals before the S arrival show up on all the three magnetic components B_x, B_y and B_z . This is a significant change making the behavior of the simulated coseismic magnetic signals in better accordance with the observation result. All the simulation results in Figs. 4a, 7 and 8 cannot explain well the observation result, especially the behavior of the coseismic B_z component which starts to show up from the P arrival (Fig. 2). Ren et al. (2015) suggested that the scattering effect probably can make the simulated coseismic B_z component behave close to the observation result. This viewpoint is now verified by our simulation result (Fig. 9a). Further checking the simulation result

in cylindrical coordinates (Fig. 9b), we find that, for the time period between P and S arrivals, evident signals exhibit on all the components of seismic, electric and magnetic wave-fields (except the vertical electric component which is usually not considered). The signal strength level of every component of seismic, electric, and magnetic wave-fields shown by Fig. 9 is generally close to that shown by Fig. 2. Hence, the signal strength ratio of x - to y -component or r - to θ -component also agrees with the observation result in a better way.

Generally speaking, regarding the general characteristics of the observation result, such as the signal showing up time and the signal strength ratio of x - to y -component or r - to θ -component, the simulation result of the scattering effect (Fig. 9) apparently shows a better agreement with the observation result (Fig. 2) than those displayed in Figs. 4a, 7 and 8. However, one difference still lies between the simulation and observation results. In the simulation result (Fig. 9), the signal strength level of B_z component is close to that of B_x or B_y component. However, in the observation result (Fig. 2), the B_z component has a signal strength level about 5 times higher than that of B_x or B_y component. One possible explanation is that the observation instrument may have tilted while being placed or after the occurrence of the foreshock or mainshock. The landform of the observation area presumably is complicated and has not been taken into account in our numerical simulation. At present, the influence of landform (topographic) variation on coseismic EM signals is unknown. Hence, numerical simulation studies on 3D models with the presence of landforms can be a future work. These studies may provide more comprehensive understanding to the general characteristics of coseismic EM signals.

The seismic and EM wave-fields displayed in Fig. 9 are contributed by two parts, namely, the weakened original wave-fields and the additional wave-fields resulting from the PSV-to-SH and SH-to-PSV conversions. These additional wave-fields before applying the horizontal wave-field rotation are also displayed in Cartesian (Fig. 10a) and cylindrical coordinates (Fig. 10b), respectively. The wave-fields caused by PSV-to-SH conversion can be easily differentiated from those caused by SH-to-PSV conversion in cylindrical coordinates. The v_θ, E_θ, B_r and B_z components belong to the SHTE model. Hence, they are caused by the PSV-to-SH conversion, and they start to show up from the P arrival. The v_r, v_z, E_r and B_θ components belong to the PSVTM model. Thus, they are caused by SH-to-PSV conversion. Since some parts of the SH wave are artificially converted into P and SV waves and a horizontally layered model is adopted, refracted P wave propagating along the ground surface can be generated by SH wave

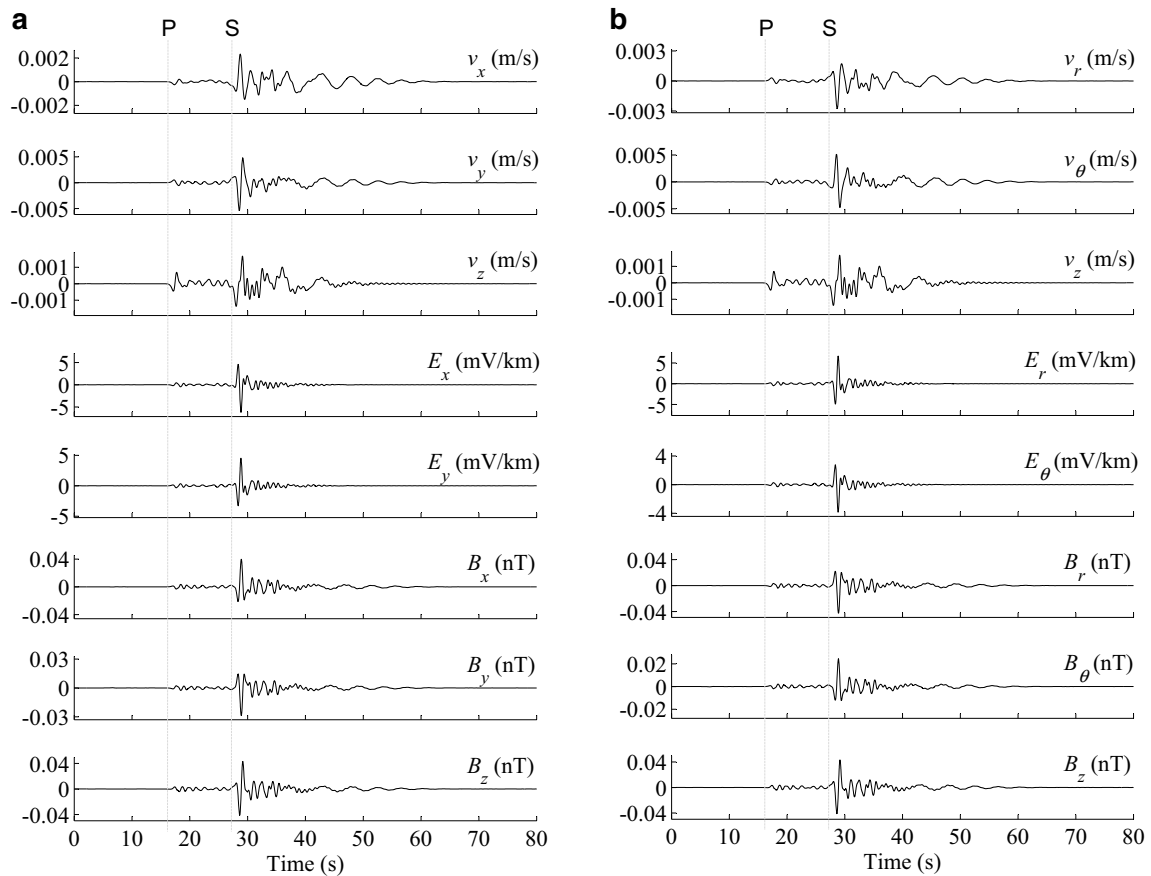


Fig. 9 Seismic and EM signals obtained by considering an artificial scattering effect. Once again, we consider the seven-layer half-space model and a receiver located at $(-80,890, 8680, 0.1)$ m. An artificial scattering effect is introduced by employing an artificial scattering conversion coefficient of $C_{st}=0.6$ and a horizontal wave-field rotation angle of 30° in the counterclockwise direction. The simulated seismic and EM wave-fields are displayed in **a** Cartesian and **b** cylindrical coordinates, respectively

arriving at the ground surface with an incident angle of $\theta_{ref} = \arcsin(V_s/V_{pf})$. This refracted P wave show up earlier than the S arrival due to the sufficiently long epicentral distance. Therefore, the v_r , v_z , E_r and B_θ components start to show up later than the P arrival but earlier than the S arrival. The weak signals that show up around 6–14 s in the B_θ component (Fig. 10b) are interfacial radiation EM waves (Haartsen and Pride 1997; Garambois and Dietrich 2002; Butler et al. 2018). Their signal strengths are generally below the level of 0.0001 nT. Thus, they can be too weak to be observed in the real case.

Influences of C_{st} and aquifer thickness on coseismic EM signals

The simulated coseismic EM signals in Fig. 9 are contributed by evanescent EM waves, whose sensitivity to media properties was numerically investigated by Ren et al. (2016b). They found that the evanescent EM waves

are sensitive to some media properties, such as porosity, salinity and fluid viscosity. Therefore, we can infer that these media properties should evidently affect the coseismic EM signals shown in Fig. 9. In the following context, we investigate two others factors that were not considered by Ren et al. (2016b): artificial scattering conversion coefficient, which is proposed in the current work, and aquifer thickness.

We conduct numerical simulations on the seven-layer half-space model by adopting artificial scattering conversion coefficient C_{st} with different values of 0, 0.2, 0.4, 0.6 and 0.8 to investigate the variations of seismic and EM wave-field amplitudes. Figure 11 shows the absolute amplitudes of seismic and EM wave-fields simulated for the receiver located at $(-80,890, 8680, 0.1)$ m. The v_h , E_h and B_h components are the horizontal total components of seismic, electric and magnetic signals, respectively, while the v_z and B_z components are the vertical components of seismic and magnetic signals, respectively. For

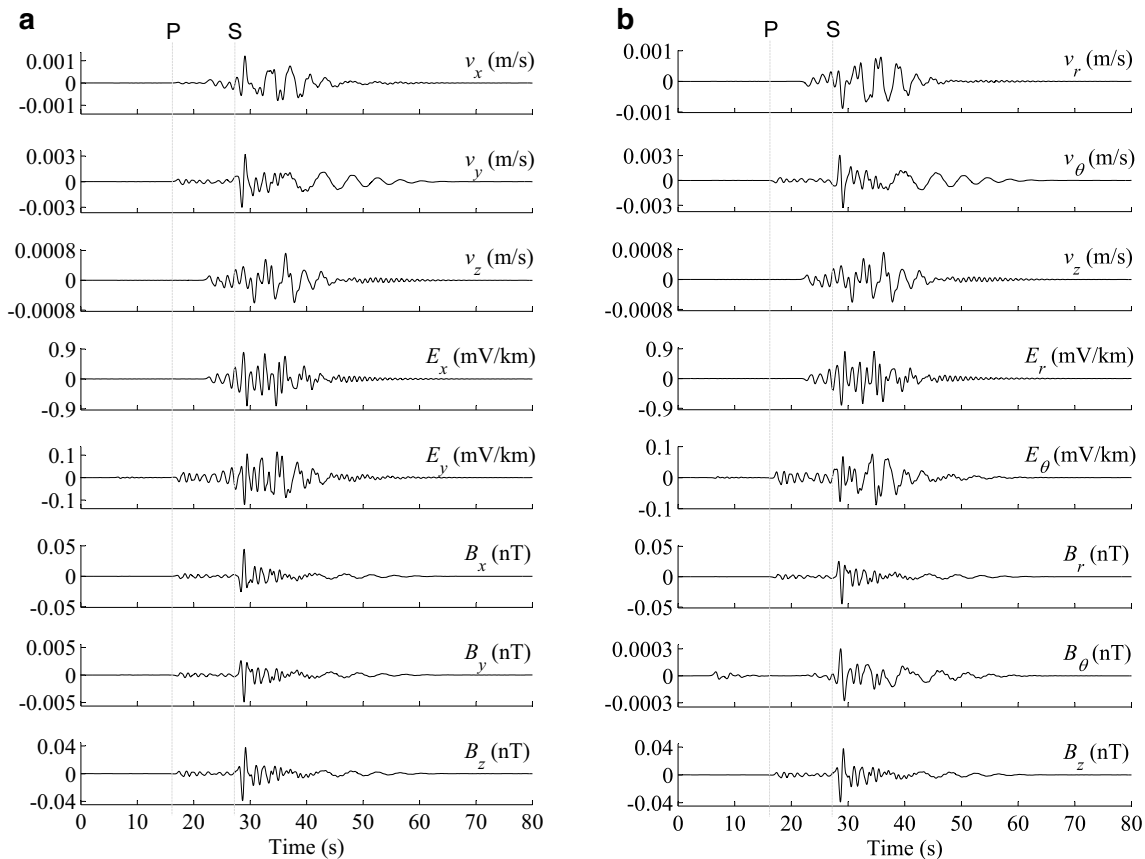


Fig. 10 Additional seismic and EM wave-fields resulting from the artificial scattering effect. We consider the seven-layer half-space model, the receiver located at $(-80, 890, 8680, 0.1)$ m and an artificial scattering effect with an artificial scattering conversion coefficient of $C_{st}=0.6$. These are the wave-fields before applying the horizontal wave-field rotation. They are caused by PSV-to-SH and SH-to-PSV conversions

all the components shown in Fig. 11, the signals before and after the time of $t=27$ s are separately displayed because their signal strength levels are different. The influence of the artificial scattering conversion coefficient on the coseismic magnetic signals is most significant. The strengths of the coseismic magnetic signals dramatically increase for higher values of C_{st} . This variation trend has a good agreement on all the coseismic magnetic signals showing up at different times. Hence, the coseismic magnetic signals observed during earthquakes may have some information on the scattering effect in the observation area. The strengths of the coseismic electric signals generally decrease for higher values of C_{st} . However, the variation extent of the coseismic electric signals is less dramatic than that of the coseismic magnetic signals. In additions, for some time periods, such as nearby $t=26.7$ or 34.5 s, the strengths of the coseismic electric signals seem to show increase variation trend for higher values of C_{st} . For seismic signals, the strength variation extent is also less dramatic than that of the coseismic magnetic signals, and a consistent variation trend is not apparent.

The influence of the aquifer thickness on the coseismic EM signals is investigated by performing numerical simulation on a modified seven-layer half-space model wherein the thickness of the aquifer (which is the second layer consisting of water-saturated porous material) is modified and the thicknesses of other layers are unchanged. An artificial scattering conversion coefficient of $C_{st}=0.6$ is adopted. Figure 12 shows the absolute amplitudes of horizontal total components and vertical components of the seismic and EM wave-fields when the aquifer thickness h is set to be 30, 80, 130, 180 or 230 m. Again, the signals before and after the time of $t=27$ s are separately displayed due to their different signal strength levels. All the seismic, electric and magnetic signals are affected by the aquifer thickness. However, the variations of seismic signals are less dramatic than those of electric or magnetic signals. Either the electric or magnetic signals show a general variation trend of stronger signal strength for thicker aquifer. This result can be understood as follows. For the used seven-layer half-space model, the coseismic EM signals recorded by the receiver nearby the ground surface are contributed

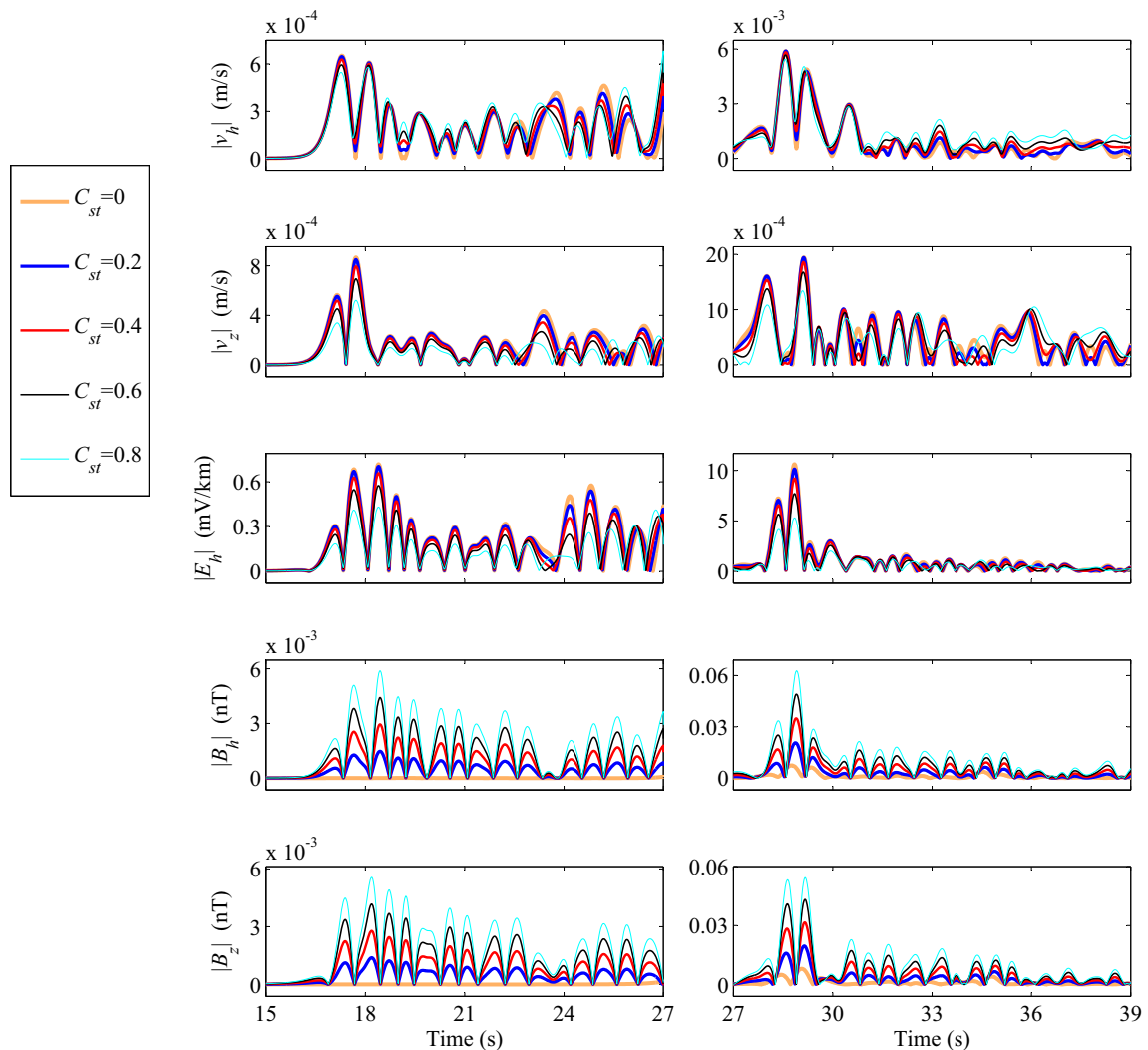


Fig. 11 Influence of scattering effect on the amplitudes of seismic and EM wave-fields. We calculate the absolute amplitudes of horizontal total components and vertical components of the seismic and EM wave-fields simulated for the receiver located at $(-80, 890, 0.1)$ m in the seven-layer half-space model when different artificial scattering conversion coefficients $C_{st} = 0, 0.2, 0.4, 0.6$ and 0.8 are adopted

by two parts of evanescent EM waves, which originate from the seismoelectric conversions taking place at the aquifer's upper and lower interfaces. These two parts of evanescent EM waves trend to counterbalance one another. However, they have different amplitude decay extents because the aquifer's upper and lower interfaces apparently are located at different depths. When the aquifer is thicker, which means the aquifer's lower interface is located at a deeper depth, the evanescent EM waves originating from the aquifer's lower interface exhibit more amplitude decay and thereby have a lower signal strength level. Consequently, they counterbalance a less portion of the evanescent EM waves originating from the aquifer's upper interface. Thus, the coseismic EM signals contributed by these two parts of evanescent EM waves finally show a higher signal strength

level. An opposite situation, that is, coseismic EM signals with a lower strength level, occurs when the aquifer is thinner. The simulation result displayed in Fig. 12 suggests that the coseismic EM signals are more sensitive to the aquifer thickness than the seismic waves.

Discussion

The scattering effect is added into our numerical simulations in a simple, rough and mandatory manner. On this basis, we use the term "artificial scattering effect". Although it cannot lead to precise results, PSV-to-SH and SH-to-PSV conversions, which exist due to the scattering effect, can now be included in our numerical simulations, and the simulation results can fit the observation data better, especially for the coseismic magnetic signals.

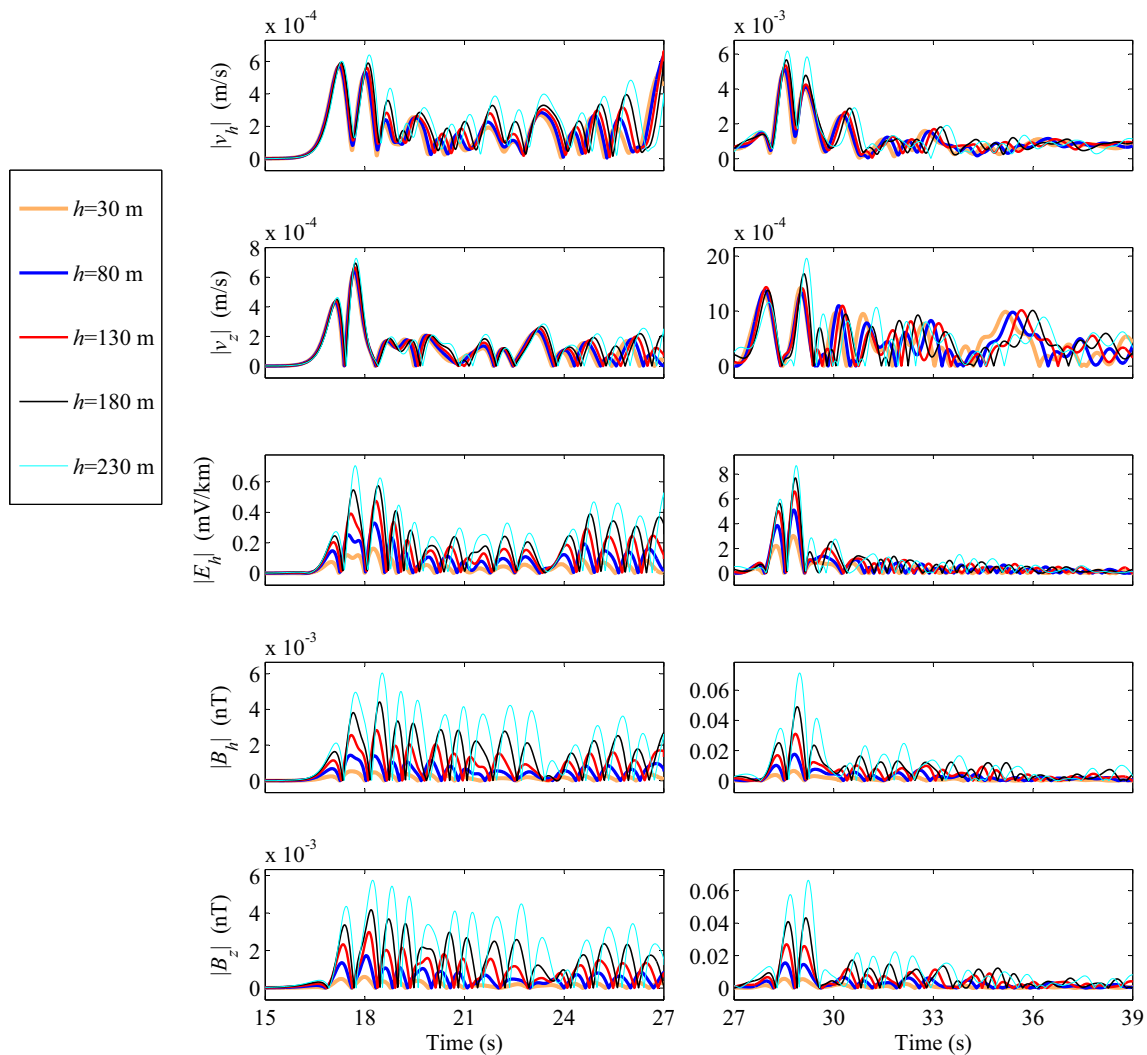


Fig. 12 Influence of aquifer thickness on the amplitudes of seismic and EM wave-fields. We calculate the absolute amplitudes of horizontal total components and vertical components of the seismic and EM wave-fields simulated for the receiver located at $(-80, 890, 8680, 0.1)$ m in the (modified) seven-layer half-space models, where the aquifer thickness is set to be $h = 30, 80, 130, 180$ or 230 m, respectively. The artificial scattering effect is considered, and the artificial scattering conversion coefficient is set as $C_{st} = 0.6$

Therefore, we can arrive at a preliminary conclusion that the scattering effect probably plays an important role in generating coseismic EM signals. However, we still need further work for a grounded conclusion. Further efforts to simulate coseismic EM signals by strictly considering the scattering effect may be significant to the proper understanding of coseismic EM phenomena. One potential tool for such kind of simulation is the curvilinear grid finite-difference method, which has been recently applied to solve the governing equation of poroelastic waves in porous media for 2D case (Sun et al. 2019). One advantage of this method is that it can well fit non-planar interfaces, such as a topographic free surface which the ground surface of the Iwo-yama volcanic area can be

considered. This method can handle the scattering effect strictly and naturally and generate precise numerical results. Applying this method to model the seismic and EM signals in 3D porous media by solving the governing equations of Pride's theory (Pride 1994) can be a future work.

In addition to electrokinetic effect, some other mechanisms may also contribute to coseismic EM signals. The motional induction effect, which was once called the seismic dynamo effect (Honkura et al. 2000; Matsushima et al. 2002), assumes the electrically conducting crust vibrating under the earth's magnetic field can cause motional EM induction. It has been taken as a possible generation mechanism of coseismic EM signals (Honkura et al.

2000; Matsushima et al. 2002; Yamazaki 2012). Recently, Gao et al. (2019) modeled such effect for a 2D layered model. Although coseismic magnetic signals appearing at the arrival time of both P and S waves were obtained for a receiver located nearby the ground surface, the signal strengths of the simulated magnetic induction intensity are generally at the level of 10^{-4} – 10^{-7} nT (Gao et al. 2019). Such weak magnetic signal can be hardly recorded in the presence of magnetic noise in real situations. Given that Gao et al. (2019) only considered 2D case, whether the motional induction effect can generate observable coseismic magnetic signals in the 3D case can be a future work deserving further efforts. Jiang et al. (2018) showed that the rotation-induced magnetic field in a coil magnetometer by seismic waves can contribute to the recorded coseismic magnetic signals. Such kind of magnetic signals probably should be removed from the data to eliminate instrumental response and to obtain the real coseismic magnetic signals.

Conclusions

Coseismic EM signals were recorded by the observation stations located in Iwo-yama area during the 2016 Kumamoto earthquake. A $M5.4$ aftershock which occurred about 19 min after the mainshock is chosen as our research target. The observation result suggests that the coseismic EM signals started to show up from the arrival time of P wave and existed for the whole duration time of seismic waves. This is a general characteristic which also has been shown by coseismic EM signals observed for other natural earthquakes (Nagao et al. 2000; Karakelian et al. 2002a, b; Matsushima et al. 2002; Tang et al. 2010; Gao et al. 2016). In this work, we try to explain the coseismic EM signals observed for the $M5.4$ aftershock by conducting numerical simulations on several different models.

At first, we adopt a water-saturated half-space porous model (Fig. 3b). The simulation result for a receiver located at $(-80, 890, 8680, 0.1)$ m shows that the arrivals of P, refracted SV–P, S and Rayleigh waves can be found on either seismic or electric signals, whereas only the arrival of S wave can be found on magnetic signals (Fig. 4a). Further investigation shows that the coseismic EM signals actually are contributed by two parts, that is, the localized EM fields and evanescent EM waves. For the B_x and B_y components, the signals synchronous with P, refracted SV–P and Rayleigh waves also exist on the localized fields as well as the evanescent waves, but they just counterbalance one another (Fig. 4b). Thus, they are missing on the total B_x and B_y components (Fig. 4a). However, due to the amplitude decay of the evanescent EM waves (Fig. 6), the coseismic magnetic signals synchronous with P, refracted SV–P and Rayleigh waves can show up again for a receiver located at a deep depth such as 0.5 km (Fig. 5). The B_z

component only shows coseismic signals synchronous with S arrival whether the receiver is located nearby the ground surface or at depths (Figs. 4, 5 and 6), because it is theoretically only induced by SH waves for a horizontally layered model (Ren et al. 2015). Then, numerical simulations are performed on a seven-layer half-space model (Fig. 3c) which is a conceptual model. The second layer consisting of water-saturated porous material is an analogy of aquifer. The other six layers, where the electrokinetic effect is inoperative, are made up of air-saturated porous material. The simulation result in Fig. 7 shows that the coseismic magnetic signals before the S arrival are still missing on B_x , B_y and B_z components when only the electrokinetic effect is considered. Thereafter, we test the surface-charge assumption (Ren et al. 2015) on the seven-layer half-space model. To some extent, the simulation result becomes close to the observation result because the signals between the P and S arrivals start to show up on B_x and B_y components. However, these signals are missing on v_θ , E_θ , B_r and B_z components (Fig. 8). The simulation results in Figs. 4, 7 and 8 all fail to explain well the observation result (Fig. 2), because the showing up time of coseismic magnetic signals significantly differs from the observation. Another difference is the signal strength ratio of x - to y - (or r - to θ -) component. Except for the magnetic signals simulated for the surface-charge assumption, the simulation results in Figs. 4, 7 and 8 generally have a higher ratio than the observation result.

The observation stations were located in a volcanic area. Therefore, the scattering effect probably played an important role in generating coseismic EM signals. On this basis, we introduce an artificial scattering effect into our numerical simulations to investigate its possible influence on coseismic EM signals. The new simulation result on the seven-layer half-space model with the artificial scattering effect agrees well with the observation result on both the signal's showing up time and the signal strength ratio of x - to y - (or r - to θ -) component (Fig. 9). Thus, the combination of electrokinetic effect and scattering effect may be a reasonable explanation to the coseismic EM signals observed during natural earthquakes. The influences of the artificial scattering conversion coefficient and the aquifer thickness on coseismic EM signals are further investigated (Figs. 11 and 12). The strengths of coseismic magnetic signals are dramatically enhanced for higher values of artificial scattering conversion coefficients, and the coseismic EM signals show higher strength levels for a thicker aquifer. Coseismic electric and/or magnetic signals are more sensitive to the artificial scattering conversion coefficient and the aquifer thickness than seismic signals. Thus, the EM observation can provide some information on the earth media, which the seismic observation can hardly provide.

Abbreviations

EM: electromagnetic; LAC: Luco–Apsel–Chen; GRM: generalized reflection and transmission method; MT: magnetotelluric; ERI: Earthquake Research Institute; JMA: Japan Meteorological Agency; NIED: National Research Institute for Earth Science and Disaster Resilience.

Acknowledgements

The authors acknowledge the use of Focal Mechanism Catalog from NIED. The main part of this work was carried out when Dr. Ren was visiting ERI, The University of Tokyo in 2017. Dr. Ren very much appreciates the warm-hearted help and important supports from International Research Promotion Office of ERI during that period. All the authors appreciate the excellent review work of the two anonymous reviewers.

Authors' contributions

MU, KA, KT, WK, KS, TK, TO and AW carried out the field observation and analyzed the data. Y-CS, HR, QH, JR and XC carried out the numerical simulations. All authors read and approved the final manuscript.

Funding

This study was supported by the National Natural Science Foundation of China (Grant numbers 41674074, 41874082, 41790465 and 41904046). This study was also supported by the Ministry of Education, Culture, Sports, Science and Technology (MEXT) of Japan, under its "Earthquake and Volcano Hazards Observation and Research Program" and "Integrated Program for Next Generation Volcano Research and Human Resource Development".

Availability of data and materials

The field observation data shown in this article are available from ERI. The numerical simulation data are available from Dr. Hengxin Ren (renhx@sustech.edu.cn).

Ethics approval and consent to participate

Not applicable.

Consent for publication

Not applicable.

Competing interests

The authors declare that they have no competing interests.

Author details

¹ Department of Earth and Space Sciences, Southern University of Science and Technology, Shenzhen, Guangdong 518055, China. ² Earthquake Research Institute, The University of Tokyo, Tokyo 113-0032, Japan. ³ Department of Geophysics, School of Earth and Space Sciences, Peking University, Beijing 100871, China. ⁴ Institute of Seismology and Volcanology, Kyushu University, Fukuoka, Japan. ⁵ Graduate School of Science, Kyushu University, Fukuoka, Japan. ⁶ Present Address: Fukuoka Regional Headquarters, Japan Meteorological Agency, Fukuoka, Japan. ⁷ School of Science, Tokyo Institute of Technology, Tokyo, Japan. ⁸ Present Address: Geological Survey of Japan, National Institute of Advanced Industrial Science and Technology, Tsukuba, Japan. ⁹ Present Address: Oyo Co., Saitama, Japan.

Appendix A: Seismoelectric modeling in layered porous media

For a layered porous model with a source in the s th layer, the scalar and vector wave-fields involved in the governing Eqs. (1)–(7) can be expanded through a set of scalar and vector function basis (see Appendix B) expressed in cylindrical coordinates. Then, one will obtain two independent sets of linear ordinary differential equations, which correspond to the case of SHTE (where SH waves are coupled to EM fields of transversely polarized electric mode) and the case of PSVTM (where P and SV waves are coupled to the EM

fields of transversely polarized magnetic mode). For the wave-fields in the j th layer bounded by interfaces of $z = z^{(j-1)}$ and $z = z^{(j)}$, both cases can be written in the following form:

$$\frac{\partial}{\partial z} \mathbf{y}^{(j)}(z) = \mathbf{A}^{(j)} \mathbf{y}^{(j)}(z) + \delta_{j,s} \mathbf{S}(z), \quad (27)$$

where $z^{(j-1)} < z < z^{(j)}$, \mathbf{y} is a vector that comprises the wave-fields' expansion coefficients, \mathbf{S} is the vector of source information, \mathbf{A} is a matrix that comprises the information of medium properties and horizontal partial derivatives, and $\delta_{j,s}$ is the Kronecker delta function. The \mathbf{y} vectors of the two cases are written as:

$$\mathbf{y}^{\text{SHTE}} = [u_{T,m} \ \tau_{T,m} \ H_{S,m} \ E_{T,m}]^T, \quad (28)$$

$$\mathbf{y}^{\text{PSVTM}} = [u_{S,m} \ u_{R,m} \ w_{R,m} \ \tau_{S,m} \ \tau_{R,m} \ P_m \ H_{T,m} \ E_{S,m}]^T, \quad (29)$$

where $u_{T,m}$, $u_{S,m}$, $u_{R,m}$, $w_{R,m}$, $\tau_{T,m}$, $\tau_{S,m}$, $\tau_{R,m}$, $H_{T,m}$, $H_{S,m}$, $E_{T,m}$, $E_{S,m}$ and P_m are the corresponding expansion coefficients of unknown vector functions \mathbf{u} , \mathbf{w} , $\boldsymbol{\tau}$, \mathbf{H} , \mathbf{E} , and the unknown pore-fluid pressure P , respectively.

The general solution of Eq. (27) can be written as (Ren et al. 2012):

$$\mathbf{y}^{(j)}(z) = \boldsymbol{\Theta}^{(j)} \boldsymbol{\Lambda}^{(j)}(z) [\mathbf{a}^{(j)} + \delta_{j,s} \mathbf{b}(z)], \quad (30)$$

where \mathbf{a} is a to-be-solved vector that contains the adjusted wave-field amplitudes and \mathbf{b} is the source term vector. The two matrices $\boldsymbol{\Theta}$ and $\boldsymbol{\Lambda}(z)$ are related to the eigen decomposition of matrix \mathbf{A} as follows (Ren et al. 2012):

$$\boldsymbol{\Theta}^{(j)} = [\mathbf{e}_1 \ \mathbf{e}_2 \ \dots \ \mathbf{e}_m \ \mathbf{e}_{m+1} \ \mathbf{e}_{m+2} \ \dots \ \mathbf{e}_{2m}], \quad (31)$$

$$\boldsymbol{\Lambda}^{(j)}(z) = \begin{bmatrix} \boldsymbol{\Lambda}_d^{(j)}(z) & \\ & \boldsymbol{\Lambda}_u^{(j)}(z) \end{bmatrix}, \quad (32)$$

$$\begin{cases} \boldsymbol{\Lambda}_d^{(j)}(z) = \text{diag}\{e^{-\lambda_1[z-z^{(j-1)}]}, e^{-\lambda_2[z-z^{(j-1)}]}, \dots, e^{-\lambda_m[z-z^{(j-1)}]}\} \\ \boldsymbol{\Lambda}_u^{(j)}(z) = \text{diag}\{e^{-\lambda_1[z^{(j)}-z]}, e^{-\lambda_2[z^{(j)}-z]}, \dots, e^{-\lambda_m[z^{(j)}-z]}\} \end{cases}, \quad (33)$$

where $\boldsymbol{\Lambda}_d^{(j)} \mathbf{e}_i = -\lambda_i \mathbf{e}_i$ ($i = 1, 2, \dots, m$), $\boldsymbol{\Lambda}_u^{(j)} \mathbf{e}_i = \lambda_i \mathbf{e}_i$ ($i = m+1, m+2, \dots, 2m$), namely, $\pm \lambda_i$ ($i = 1, 2, \dots, m$) and \mathbf{e}_i ($i = 1, 2, \dots, 2m$) are the eigen-values and eigen-vectors of matrix $\mathbf{A}^{(j)}$, respectively. For the wave propagation problem, the eigen-values, which represent the vertical wavenumbers, always show up in pairs because the existence of down-going and up-going waves with same horizontal wave-number is always reasonable. Thus, $\boldsymbol{\Lambda}^{(j)}(z)$ can be expressed in the form of Eqs. (32) and (33). For SHTE

case, we obtain $m=2$ pairs of eigen-values, $\pm\lambda_i$ ($i=1,2$). For PSVTM case, we obtain $m=4$ pairs of eigen-values, $\pm\lambda_i$ ($i=1,2,3,4$). We define $\text{Re}(\lambda_i) > 0$. Thus, the two diagonal matrices $\mathbf{\Lambda}_d(z)$ and $\mathbf{\Lambda}_u(z)$ correspond to down-going and up-going waves, respectively (Ren et al. 2012, 2016a). It should be emphasized that, in Eq. (33), the introduction of extra exponential factors $\exp(\lambda_i z^{(j-1)})$ and $\exp(-\lambda_i z^{(j)})$ is an important pretreatment of the LAC GRTM. It guarantees that all the diagonal elements in the matrix $\mathbf{\Lambda}^{(j)}(z)$ satisfy $|\exp[-\lambda_i(z - z^{(j-1)})]| \leq 1$ or $|\exp[-\lambda_i(z^{(j)} - z)]| \leq 1$, which provides a good stability in the numerical simulation section.

$$f_m(z, k, \omega) = \int_0^{2\pi} \int_0^{\infty} F(r, \theta, z, \omega) [Y_k^m(r, \theta)]^* r dr d\theta, \quad (36)$$

where the symbol $*$ indicates the complex conjugate.

For a vector function, we take the following set of vector functions as basis,

$$\begin{cases} \mathbf{T}_k^m(r, \theta) = k^{-1} \nabla \times [\mathbf{e}_z Y_k^m(r, \theta)] \\ \mathbf{S}_k^m(r, \theta) = k^{-1} \nabla Y_k^m(r, \theta) \\ \mathbf{R}_k^m(r, \theta) = -\mathbf{e}_z Y_k^m(r, \theta) \end{cases}, \quad (37)$$

where \mathbf{e}_z is the unit vector in z direction. Then, an arbitrary vector function, say $\mathbf{A}(r, \theta, z, \omega)$, can be expanded as follows:

$$\begin{aligned} \mathbf{A}(r, \theta, z, \omega) = \frac{1}{2\pi} \sum_{m=-\infty}^{+\infty} \int_0^{+\infty} \{ & A_{T,m}(z, k, \omega) \mathbf{T}_k^m(r, \theta) \\ & + A_{S,m}(z, k, \omega) \mathbf{S}_k^m(r, \theta) + A_{R,m}(z, k, \omega) \mathbf{R}_k^m(r, \theta) \} k dk, \end{aligned} \quad (38)$$

The vector \mathbf{a} will be determined by the LAC GRTM (Ren et al. 2012). After obtaining the wave-field solutions in the frequency–wavenumber domain, we can transform them back to the space–time domain by using the well-known discrete wavenumber method (Bouchon and Aki 1977; Bouchon 1981), which virtually introduces a spatial periodicity of sources to discretize the radiated wave-fields and imposes the discrete Fourier transform with complex frequencies to perform the integration over the frequency domain.

Appendix B: A set of scalar and vector function basis

The scalar function basis is

$$Y_k^m(r, \theta) = J_m(kr) e^{im\theta}, \quad (m = 0, \pm 1, \pm 2, \dots), \quad (34)$$

where $J_m(kr)$ is a Bessel function of order m . An arbitrary scalar function $F(r, \theta, z, \omega)$ can be expanded as follows:

$$F(r, \theta, z, \omega) = \frac{1}{2\pi} \sum_{m=-\infty}^{+\infty} \int_0^{+\infty} f_m(z, k, \omega) Y_k^m(r, \theta) k dk, \quad (35)$$

where $f_m(z, k, \omega)$ is the expansion coefficient of $F(r, \theta, z, \omega)$, which can be evaluated as follows:

where $A_{T,m}$, $A_{S,m}$ and $A_{R,m}$ are the expansion coefficients, which can be evaluated by the following formulas:

$$A_{T,m}(z, k, \omega) = \int_0^{2\pi} \int_0^{\infty} \mathbf{A}(r, \theta, z, \omega) \cdot [\mathbf{T}_k^m(r, \theta)]^* r dr d\theta, \quad (39)$$

$$A_{S,m}(z, k, \omega) = \int_0^{2\pi} \int_0^{\infty} \mathbf{A}(r, \theta, z, \omega) \cdot [\mathbf{S}_k^m(r, \theta)]^* r dr d\theta, \quad (40)$$

$$A_{R,m}(z, k, \omega) = \int_0^{2\pi} \int_0^{\infty} \mathbf{A}(r, \theta, z, \omega) \cdot [\mathbf{R}_k^m(r, \theta)]^* r dr d\theta. \quad (41)$$

Received: 4 September 2019 Accepted: 11 December 2019
Published online: 27 December 2019

References

- Aki K (1969) Analysis of seismic coda of local earthquakes as scattered waves. *J Geophys Res* 74:615–631
- Aki K (1973) Scattering of P waves under the Montana LASA. *J Geophys Res* 78:1334–1346
- Aki K (1980) Scattering and attenuation of shear waves in the lithosphere. *J Geophys Res* 85:6496–6504

- Aki K, Chouet B (1975) Origin of coda waves: source, attenuation, and scattering effects. *J Geophys Res* 80:3322–3342
- Bouchon M (1981) A simple method to calculate green-functions for elastic layered media. *Bull Seismol Soc Am* 71(4):959–971
- Bouchon M, Aki K (1977) Discrete wave-number representation of seismic-source wave fields. *Bull Seismol Soc Am* 67(2):259–277
- Butler KE, Kulesa B, Pugin A (2018) Multimode seismoelectric phenomena generated using explosive and vibroseis sources. *Geophys J Int* 213(2):836–850. <https://doi.org/10.1093/gji/ggy017>
- Chen X (1993) A systematic and efficient method for computing seismic normal modes in layered half-space. *Geophys J Int* 115(2):391–409. <https://doi.org/10.1111/j.1365-246X.1993.tb01194.x>
- Chen X (2007) Generation and propagation of seismic SH waves in multi-layered media with irregular interfaces. *Adv Geophys* 48:191–264. [https://doi.org/10.1016/S0065-2687\(06\)48004-3](https://doi.org/10.1016/S0065-2687(06)48004-3)
- Davis JA, James RO, Leckie JO (1978) Surface ionization and complexation at the oxide/water interface: I. Computation of electrical double layer properties in simple electrolytes. *J Colloid Interf Sci* 63(3):480–499. [https://doi.org/10.1016/S0021-9797\(78\)80009-5](https://doi.org/10.1016/S0021-9797(78)80009-5)
- Dietrich M, Devi MS, Garambois S, Brito D, Bordes C (2018) A novel approach for seismoelectric measurements using multielectrode arrangements—I: theory and numerical experiments. *Geophys J Int* 215(1):61–80. <https://doi.org/10.1093/gji/ggy269>
- Dzieren L, Thorwart M, Rabbal W, Ritter O (2019) Quantifying interface responses with seismoelectric spectral ratios. *Geophys J Int* 217(1):108–121. <https://doi.org/10.1093/gji/ggz010>
- Frenkel J (1944) On tire theory of seismic and seismoelectric phenomena in a moist soil. *J Phys USSR* 8:230–241
- Fujinawa Y, Noda Y (2015) Characteristics of seismoelectric wave fields associated with natural microcracks. *Pure Appl Geophys* 172:197–614
- Fujinawa Y, Takahashi K, Noda Y, Iitaka H, Yazaki S (2011) Remote detection of the electric field change induced at the seismic wave front from the start of fault rupturing. *Int J Geophys* 2011:1–11. <https://doi.org/10.1155/2011/752193>
- Gao Y, Harris JM, Wen J, Huang Y, Twardzik C, Chen X, Hu H (2016) Modeling of the coseismic electromagnetic fields observed during the 2004 M_w 6.0 Parkfield earthquake. *Geophys Res Lett*. <https://doi.org/10.1002/2015JG1067183>
- Gao Y, Wang D, Wen J, Hu H, Chen X, Yao C (2019) Electromagnetic responses to an earthquake source due to the motional induction effect in a 2-D layered model. *Geophys J Int* 219:563–593
- Garambois S, Dietrich M (2002) Full waveform numerical simulations of seismo-electromagnetic wave conversions in fluid-saturated stratified porous media. *J Geophys Res Solid Earth* 107:B7. <https://doi.org/10.1029/2001jB000316>
- Ge Z, Chen X (2008) An efficient approach for simulating wave propagation with the boundary element method in multilayered media with irregular interfaces. *Bull Seismol Soc Am* 98(6):3007–3016. <https://doi.org/10.1785/0120080920>
- Gershenson NI, Gokhberg MB, Yunga SL (1993) On the electromagnetic field of an earthquake focus. *Phys Earth Planet Interiors* 77:13–19
- Gershenson NI, Bambakidis G, Ternovskiy I (2014) Coseismic electromagnetic field due to the electrokinetic effect. *Geophysics* 79(5):E217–E229
- Haartsen MW, Pride SR (1997) Electrostatic waves from point sources in layered media. *J Geophys Res-Solid Earth*. 102:B11. <https://doi.org/10.1029/97JB02936>
- Haines SS, Pride SR (2006) Seismoelectric numerical modeling on a grid. *Geophysics* 71(6):N57–N65. <https://doi.org/10.1190/1.2357789>
- Han P, Hattori K, Huang Q, Hirano T, Ishiguro Y, Yoshino C, Febriani F (2011) Evaluation of ULF electromagnetic phenomena associated with the 2000 Izu Islands earthquake swarm by wavelet transform analysis. *Nat Hazards Earth Syst Sci* 11(3):965–970. <https://doi.org/10.5194/nhess-11-965-2011>
- Han P, Hattori K, Hirokawa M, Zhuang J, Chen C-H, Febriani F, Yamaguchi H, Yoshino C, Liu J-Y, Yoshida S (2014) Statistical analysis of ULF seismomagnetic phenomena at Kakioka, Japan, during 2001–2010. *J Geophys Res Space Phys* 119(6):4998–5011. <https://doi.org/10.1002/2014ja019789>
- Han P, Hattori K, Xu G, Ashida R, Chen C-H, Febriani F, Yamaguchi H (2015) Further investigations of geomagnetic diurnal variations associated with the 2011 off the Pacific coast of Tohoku earthquake (M_w 9.0). *J Asian Earth Sci* 114:321–326. <https://doi.org/10.1016/j.jseae.2015.02.022>
- Han P, Hattori K, Huang Q, Hirooka S, Yoshino C (2016) Spatiotemporal characteristics of the geomagnetic diurnal variation anomalies prior to the 2011 Tohoku earthquake (M_w 9.0) and the possible coupling of multiple pre-earthquake phenomena. *J Asian Earth Sci* 129:13–21. <https://doi.org/10.1016/j.jseae.2016.07.011>
- Han P, Hattori K, Zhuang J, Chen C-H, Liu J-Y, Yoshida S (2017) Evaluation of ULF seismo-magnetic phenomena in Kakioka, Japan by using Molchan's error diagram. *Geophys J Int* 208(1):482–490. <https://doi.org/10.1093/gji/ggw404>
- Hattori K, Han P, Yoshino C, Febriani F, Yamaguchi H, Chen C-H (2013) Investigation of ULF seismo-magnetic phenomena in Kanto, Japan during 2000–2010: case studies and statistical studies. *Surv Geophys* 34(3):293–316. <https://doi.org/10.1007/s10712-012-9215-x>
- Honkura Y, İşıkara AM, Oshiman N, Ito A, Üçer B, Barış Ş, Tunçer MK, Matsushima M, Pektaş R, Çelik C, Tank SB, Takahashi F, Nakanishi M, Yoshimura R, Ikeda Y, Komut T (2000) Preliminary results of multidisciplinary observations before, during and after the Kocaeli (Izmit) earthquake in the western part of the North Anatolian Fault Zone. *Earth Planets Space* 52(4):293–298. <https://doi.org/10.1186/BF03351638>
- Honkura Y, Ogawa Y, Matsushima M, Nagaoka S, Ujihara N, Yamawaki T (2009) A model for observed circular polarized electric fields coincident with the passage of large seismic waves. *J Geophys Res Solid Earth*. <https://doi.org/10.1029/2008jb006117>
- Hu H, Gao Y (2011) Electromagnetic field generated by a finite fault due to electrokinetic effect. *J Geophys Res* 116:B08302
- Huang Q (2002) One possible generation mechanism of co-seismic electric signals. *Proc Jpn Acad Ser B* 78(7):173–178. <https://doi.org/10.2183/pjab.78.173>
- Huang Q (2011a) Rethinking earthquake-related DC-ULF electromagnetic phenomena: towards a physics-based approach. *Nat Hazards Earth Syst Sci* 11(11):2941–2949. <https://doi.org/10.5194/nhess-11-2941-2011>
- Huang Q (2011b) Retrospective investigation of geophysical data possibly associated with the M(s)8.0 Wenchuan earthquake in Sichuan, China. *J Asian Earth Sci* 41:421–427. <https://doi.org/10.1016/j.jseae.2010.05.014>
- Huang Q, Ren H, Zhang D, Chen YJ (2015) Medium effect on the characteristics of the coupled seismic and electromagnetic signals. *Proc Jpn Acad Ser B* 91(1):17–24. <https://doi.org/10.2183/pjab.91.17>
- Jiang L, Xu Y, Zhu L, Liu Y, Li D, Huang R (2018) Rotation-induced magnetic field in a coil magnetometer generated by seismic waves. *Geophys J Int* 212(2):743–759
- Johnston MJS (1997) Review of electric and magnetic fields accompanying seismic and volcanic activity. *Surv Geophys* 18:441–475
- Johnston MJS, Mueller RJ (1987) Seismomagnetic observation during the 8 July 1986 magnitude 5.9 North Palm-Spring earthquake. *Science* 237:1201–1203. <https://doi.org/10.1126/science.237.4819.1201>
- Karakelian D, Beroza GC, Klemperer SL, Fraser-Smith AC (2002a) Analysis of ultralow-frequency electromagnetic field measurements associated with the 1999 M 7.1 Hector Mine, California, earthquake sequence. *Bull Seismol Soc Am* 92(4):1513–1524. <https://doi.org/10.1785/0120000919>
- Karakelian D, Klemperer SL, Fraser-Smith AC, Thompson GA (2002b) Ultra-low frequency electromagnetic measurements associated with the 1998 Mw 5.1 San Juan Bautista, California earthquake and implications for mechanisms of electromagnetic earthquake precursors. *Tectonophysics* 359:65–79. [https://doi.org/10.1016/S0040-1951\(02\)00439-0](https://doi.org/10.1016/S0040-1951(02)00439-0)
- Kennett BLN (1983) Seismic wave propagation in stratified media. Cambridge University Press, New York
- Kennett BLN, Kerry NJ (1979) Seismic waves in a stratified half space. *Geophys J R Astron Soc* 57(3):557–583. <https://doi.org/10.1111/j.1365-246X.1979.tb06779.x>
- Levander AR (1990) Seismic scattering near the earth's surface. *Pure Appl Geophys* 132:21–47
- Liu J-Y, Chen C-H, Wu T-Y, Chen H-C, Hattori K, Bleier T, Kappler K (2017) Co-seismic signatures in magnetometer, geophone, and infrasound data during the Meinong Earthquake. *Terr Atmos Ocean Sci* 28(5):683–692. <https://doi.org/10.3319/tao.2017.03.05.01>
- Luco JE, Apsel RJ (1983) On the Green's function for a layered half-space: part I. *Bull Seismol Soc Am* 73(4):909–929
- Mahardika H, Revil A, Jardani A (2012) Waveform joint inversion of seismograms and electrograms for moment tensor characterization of fracking events. *Geophysics* 77(5):ID23–ID39

- Martin BE, Thomson CJ (1997) Modelling surface waves in anisotropic structures II: examples. *Phys Earth Planet Interiors* 103:253–279. [https://doi.org/10.1016/s0031-9201\(97\)00037-x](https://doi.org/10.1016/s0031-9201(97)00037-x)
- Matsushima M, Honkura Y, Oshiman N, Bariş Ş, Tunçer MK, Tank SB, Çelik C, Takahashi F, Nakanishi M, Yoshimura R, Pektaş R, Komut T, Tolak E, Ito A, Iio Y, Işıkara AM (2002) Seismoelectromagnetic effect associated with the İzmit earthquake and its aftershocks. *Bull Seismol Soc Am* 92(1):350–360. <https://doi.org/10.1785/0120000807>
- Matsushima M, Honkura Y, Kuriki M, Ogawa Y (2013) Circularly polarized electric fields associated with seismic waves generated by blasting. *Geophys J Int* 194(1):200–211. <https://doi.org/10.1093/gji/ggt110>
- Mizutani H, Ishido T, Yokokura T, Ohnishi S (1976) Electrokinetic phenomena associated with earthquakes. *Geophys Res Lett* 3:365–368
- Mueller RJ, Johnston MJS (1990) Seismomagnetic effect generated by the October 18, 1989 M_L 7.1 Loma-Prieta, California Earthquake. *Geophys Res Lett* 17(8):1231–1234. <https://doi.org/10.1029/gl017i008p01231>
- Nagao T, Orihara Y, Yamaguchi T, Takahashi I, Hattori K, Noda Y, Sayanagi K, Uyeda S (2000) Co-seismic geoelectric potential changes observed in Japan. *Geophys Res Lett* 27(10):1535–1538. <https://doi.org/10.1029/1999gl005440>
- Ogawa T, Utada H (2000) Coseismic piezoelectric effects due to a dislocation 1. An analytic far and early-time field solution in a homogeneous whole space. *Phys Earth Planet Interiors* 121:273–288
- Okubo K, Takeuchi N, Utsugi M, Yumoto K, Sasai Y (2011) Direct magnetic signals from earthquake rupturing: Iwate-Miyagi earthquake of M 7.2, Japan. *Earth Planet Sci Lett* 305:65–72
- Olson AH, Apsel RJ (1982) Finite faults and inverse theory with applications to the 1979 Imperial Valley earthquake. *Bull Seismol Soc Am* 72(6):1969–2001
- Press F (1964) Seismic wave attenuation in the crust. *J Geophys Res* 69(20):4417–4418. <https://doi.org/10.1029/JZ069i020p04417>
- Pride SR (1994) Governing equations for the coupled electromagnetics and acoustics of porous media. *Phys Rev B* 50:15678–15696. <https://doi.org/10.1103/PhysRevB.50.15678>
- Pride SR, Haartsen MW (1996) Electrostatic wave properties. *J Acoust Soc Am* 100(3):1301–1315. <https://doi.org/10.1121/1.416018>
- Pride SR, Morgan F (1991) Electrokinetic dissipation induced by seismic waves. *Geophysics* 56:914–925
- Pride SR, Moreau F, Gavrilenko P (2004) Mechanical and electrical response due to fluid-pressure equilibration following an earthquake. *J Geophys Res-Solid Earth*. 109B3. <https://doi.org/10.1029/2003JB002690>
- Ren H, Huang Q, Chen X (2010a) Analytical regularization of the high-frequency instability problem in numerical simulation of seismoelectric wave-fields in multi-layered porous media. *Chin J Geophys* 53(3):506–511. <https://doi.org/10.3969/j.issn.0001-5733.2010.03.004>
- Ren H, Huang Q, Chen X (2010b) A new numerical technique for simulating the coupled seismic and electromagnetic waves in layered porous media. *Earthq Sci* 23:167–176. <https://doi.org/10.1007/s11589-009-0071-9>
- Ren H, Chen X, Huang Q (2012) Numerical simulation of coseismic electromagnetic fields associated with seismic waves due to finite faulting in porous media. *Geophys J Int* 188(3):925–944. <https://doi.org/10.1111/j.1365-246X.2011.05309.x>
- Ren H, Wen J, Huang Q, Chen X (2015) Electrokinetic effect combined with surface-charge assumption: a possible generation mechanism of coseismic EM signals. *Geophys J Int* 200(2):835–848. <https://doi.org/10.1093/gji/ggu435>
- Ren H, Huang Q, Chen X (2016a) Existence of evanescent electromagnetic waves resulting from seismoelectric conversion at a solid-porous interface. *Geophys J Int* 204(1):147–166. <https://doi.org/10.1093/gji/ggv400>
- Ren H, Huang Q, Chen X (2016b) Numerical simulation of seismo-electromagnetic fields associated with a fault in a porous medium. *Geophys J Int* 206(1):205–220. <https://doi.org/10.1093/gji/ggw144>
- Ren H, Huang Q, Chen X (2018) Quantitative understanding on the amplitude decay characteristic of the evanescent electromagnetic waves generated by seismoelectric conversion. *Pure Appl Geophys* 175(8):2853–2879. <https://doi.org/10.1007/s00024-018-1823-z>
- Sakai H, Kobayashi T, Izumi Y, Nakayama T, Hattori K (2017) Induced change of electric self-potential and magnetic field at the artificial explosion. *Electr Commun Jpn* 100(3):68–75. <https://doi.org/10.1002/ecj.11942>
- Skordas E, Kapiris P, Bogris N, Varotsos P (2000) Field experimentation on the detectability of co-seismic electric signals. *Proc Jpn Acad Ser B* 76(4):51–56. <https://doi.org/10.2183/pjab.76.51>
- Sun Y-C, Ren H, Zheng X-Z, Li N, Zhang W, Huang Q, Chen X (2019) 2-D poroelastic wave modelling with a topographic free surface by the curvilinear grid finite-difference method. *Geophys J Int* 218(3):1961–1982. <https://doi.org/10.1093/gji/ggz263>
- Tang J, Zhan Y, Wang L-F, Dong Z-Y, Zhao G-Z, Xu J-L (2010) Electromagnetic coseismic effect associated with aftershock of Wenchuan $M(s)$ 8.0 earthquake. *Chin J Geophys* 53(3):526–534. <https://doi.org/10.3969/j.issn.0001-5733.2010.03.006>
- Tsukamoto K, Aizawa K, Chiba K, Kanda W, Uyeshima M, Koyama T, Utsugi M, Seki K, Kishita T (2018) Three-dimensional resistivity structure of Iwo-yama volcano, Kirishima Volcanic Complex, Japan: relationship to shallow seismicity, surface uplift, and a small phreatic eruption. *Geophys Res Lett* 45(2):12821–12828. <https://doi.org/10.1029/2018GL080202>
- Tsutsui M (2014) Behaviors of electromagnetic waves directly excited by earthquakes. *IEEE Geosci Remote Sens Lett* 11(11):1961–1965
- Wang Q, Huang Q (2016) The spatio-temporal characteristics of geomagnetic induction vectors in North China. *Chin J Geophys* 59(1):215–228. <https://doi.org/10.6038/cjg20160118>
- Wu R-S (1982) Attenuation of short period seismic waves due to scattering. *Geophys Res Lett* 9:9–12
- Wu R-S, Aki K (1985) Scattering characteristics of elastic waves by an elastic heterogeneity. *Geophysics* 50:582–595
- Xu G, Han P, Huang Q, Hattori K, Febriani F, Yamaguchi H (2013) Anomalous behaviors of geomagnetic diurnal variations prior to the 2011 off the Pacific coast of Tohoku earthquake (M_w 9.0). *J Asian Earth Sci* 77:59–65. <https://doi.org/10.1016/j.jseaes.2013.08.011>
- Yamazaki K (2012) Estimation of temporal variations in the magnetic field arising from the motional induction that accompanies seismic waves at a large distance from the epicentre. *Geophys J Int* 190(3):1393–1403. <https://doi.org/10.1111/j.1365-246X.2012.05586.x>
- Yamazaki K (2013) Improved models of the piezomagnetic field for the 2011 M_w 9.0 Tohoku-oki earthquake. *Earth Planet Sci Lett* 363:9–15. <https://doi.org/10.1016/j.epsl.2012.12.019>
- Zhang D, Ren H, Huang Q (2013) Numerical simulation study of co-seismic electromagnetic signals in porous media. *Chin J Geophys* 56(8):2739–2747. <https://doi.org/10.6038/cjg20130822>

Publisher's Note

Springer Nature remains neutral with regard to jurisdictional claims in published maps and institutional affiliations.